



**HAL**  
open science

## Crust stratigraphy and heterogeneities of the first kilometers at the dichotomy boundary in western Elysium Planitia and implications for InSight lander

L. Pan, C. Quantin-Nataf, B. Tauzin, C. Michaut, M. Golombek, P. Lognonné, P. Grindrod, Benoit Langlais, T. Gudkova, I. Stepanova, et al.

### ► To cite this version:

L. Pan, C. Quantin-Nataf, B. Tauzin, C. Michaut, M. Golombek, et al.. Crust stratigraphy and heterogeneities of the first kilometers at the dichotomy boundary in western Elysium Planitia and implications for InSight lander. *Icarus*, 2020, 338, pp.113511. 10.1016/j.icarus.2019.113511 . hal-02346218

**HAL Id: hal-02346218**

**<https://hal.science/hal-02346218>**

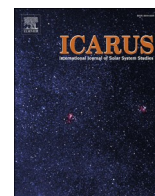
Submitted on 7 Aug 2020

**HAL** is a multi-disciplinary open access archive for the deposit and dissemination of scientific research documents, whether they are published or not. The documents may come from teaching and research institutions in France or abroad, or from public or private research centers.

L'archive ouverte pluridisciplinaire **HAL**, est destinée au dépôt et à la diffusion de documents scientifiques de niveau recherche, publiés ou non, émanant des établissements d'enseignement et de recherche français ou étrangers, des laboratoires publics ou privés.



Distributed under a Creative Commons Attribution - NonCommercial 4.0 International License



## Crust stratigraphy and heterogeneities of the first kilometers at the dichotomy boundary in western Elysium Planitia and implications for InSight lander

Lu Pan<sup>a,\*</sup>, Cathy Quantin-Nataf<sup>a</sup>, Benoit Tazuin<sup>a,b</sup>, Chloé Michaut<sup>c</sup>, Matt Golombek<sup>d</sup>, LognonnePhillipe Lognonné<sup>e</sup>, Peter Grindrod<sup>f</sup>, Benoit Langlais<sup>g</sup>, Tamara Gudkova<sup>h</sup>, Inna Stepanova<sup>h</sup>, Sébastien Rodriguez<sup>e</sup>, Antoine Lucas<sup>e</sup>

<sup>a</sup> Université de Lyon, Université Claude Bernard Lyon 1, ENS de Lyon, CNRS, UMR 5276 Laboratoire de Géologie de Lyon -Terre, Planètes, Environnement, 69622 Villeurbanne, France

<sup>b</sup> Research School of Earth Sciences, The Australian National University, Canberra, ACT 2601, Australia

<sup>c</sup> Université de Lyon, École Normale Supérieure de Lyon, UCBL, CNRS, Laboratoire de Géologie de Lyon -Terre, Planètes, Environnement, 69007 Lyon, France

<sup>d</sup> Jet Propulsion Laboratory, California Institute of Technology, Pasadena, CA 91109, United States of America

<sup>e</sup> Université de Paris, Institut de physique du globe de Paris, CNRS, F-75005 Paris, France

<sup>f</sup> The Natural History Museum at Tring Akeman Street, Tring, Hertfordshire HP23 6AP, United Kingdom of Great Britain and Northern Ireland

<sup>g</sup> Laboratoire de Planétologie et Géodynamique, Univ. Nantes, Univ. Angers, CNRS, UMR 6112, F-44000 Nantes, France

<sup>h</sup> Schmidt Institute of Physics of the Earth, Russian Academy of Sciences, B. Gruzinskaya 10, Moscow 123495, Russia

### ARTICLE INFO

#### Keywords:

Mars  
Cratering  
Geological processes  
Mineralogy  
Spectroscopy

### ABSTRACT

InSight landed on Mars on November 26, 2018, in western Elysium Planitia. The Mars crust beneath the lander is subject to complex geologic history next to the great topographic and crustal dichotomy of Mars. Understanding this part of the Martian crust in the subsurface would aid future investigations of the internal structure of the planet based on seismic datasets collected by the Seismic Experiment for Interior Structure (SEIS) instrument. Here, we investigate the subsurface structure and composition from the analysis of mineralogy and morphology of exposures in impact craters as well as on scarps and knobs in the general region of Elysium Planitia. Using a combination of orbital datasets, we identify exposures of subsurface materials with distinct composition and physical properties. We find olivine and pyroxene detections associated with small impact craters (1.5–7 km) rim in the vicinity of InSight lander, as well as in the transition unit and Elysium volcanic unit. Fe/Mg phyllosilicates have been identified in the central peak of the 51-km diameter Kalpin crater and on knobs in the transition unit between the dichotomy and the plains. In addition, eroded meter-scale layered unit subject to erosion has been identified in six impact craters to the north-east of the landing site, including Kalpin crater. Massive bedrock and layered, weak materials co-occur in the transition unit, indicating a complex origin. These results together suggest both materials with altered composition and layered deposit occur as distinct geologic units beneath the basaltic lava flow units. Through analogy with terrestrial sedimentary rocks or clay-bearing sediments, we suggest physically weak materials exist beneath the lava flow units in the general region of Elysium Planitia. The spatial distribution and continuity of these materials are unclear due to the lack of exposures within the lava flow unit where the InSight lander is located. These subsurface materials of distinct physical properties may result in increased attenuation or reverberations of seismic waves, to be collected by SEIS. The findings suggest a close investigation of the potential effects of subsurface stratigraphy on seismic data would help inform future data interpretation and understanding of the internal structure of Mars.

\* Corresponding author at: 2 rue Raphaël Dubois, Bâtiment GEODE, Villeurbanne 69622, France.

E-mail address: [lu.pan@univ-lyon1.fr](mailto:lu.pan@univ-lyon1.fr) (L. Pan).

<https://doi.org/10.1016/j.icarus.2019.113511>

Received 20 May 2019; Received in revised form 16 September 2019; Accepted 26 October 2019

Available online 31 October 2019

0019-1035/© 2019 The Authors.

Published by Elsevier Inc.

This is an open access article under the CC BY-NC-ND license

(<http://creativecommons.org/licenses/by-nc-nd/4.0/>).

### 1. Introduction

The Martian crust has been probed using the global scale topography and gravity returned from Mars Global Surveyor mission (Smith et al., 1999; Zuber et al., 2000), however, the internal 3D structure of Mars (e.g. core size, crustal thickness) still has large uncertainties. To better understand the formation and evolution of the terrestrial planets, the InSight (Interior Exploration using Seismic Investigations, Geodesy and Heat Transport) robotic lander launched on May 5, 2018 as the first mission to investigate the interior structure of Mars (Banerdt et al.,

2013, 2017) and successfully landed on November 26, 2018. The InSight lander explores the interior of Mars with a set of geophysical instruments (e.g. Banerdt et al., 2017), including the Seismic Experiment for Interior Structure (SEIS) (Lognonné et al., 2019), the Rotation and Interior Structure Experiment (RISE) (Folkner et al., 2018), and the Heat Flow and Physical Properties Package (HP<sup>3</sup>) (Spohn et al., 2018). One of the main science goals of the InSight mission is to understand the internal structure of Mars from seismic activity. The SEIS instrument is the first seismometer placed on Mars' surface and it consists of a 3-axis very broad band (VBB) instrument and a 3-axis short period (SP) instrument.

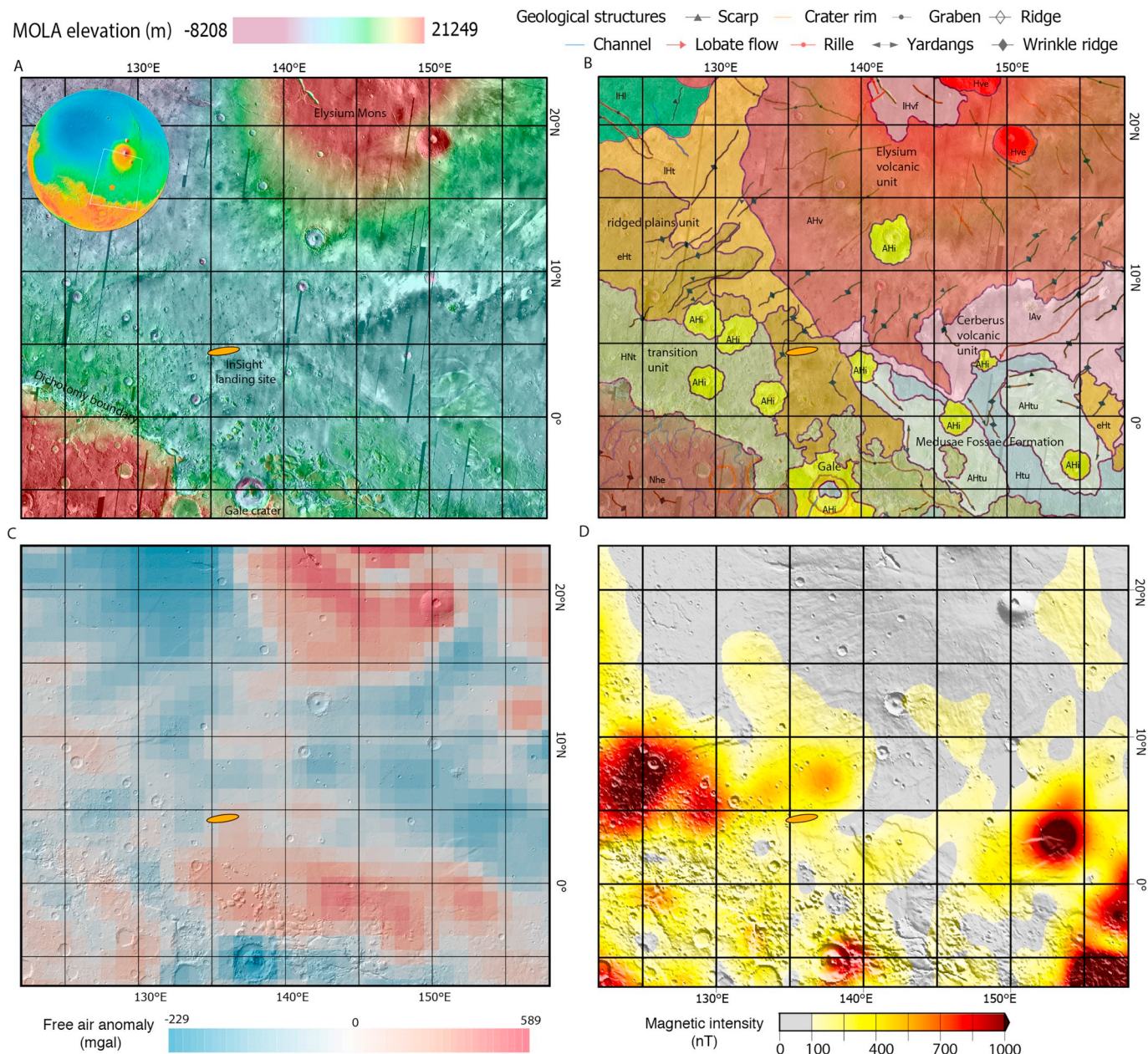


**Fig. 1.** Geologic context of InSight landing site: A) The location of InSight landing ellipse in the southwest flank of Elysium Mons volcanic terrains, north of the dichotomy boundary. Upper left corner shows a Mars globe with the highlighted region of map and landing site location. The base map is Mars THEMIS daytime infrared mosaic overlain by the topography from Mars Orbiter Laser Altimeter (MOLA), in Mars equirectangular projection. B) Geological map with the same map extent (Tanaka et al., 2014) showing the major geologic units and structures in the region. Geological unit abbreviations follow the USGS global map. Nhe: Noachian Hesperian unit; HNT: Hesperian and Noachian transition unit; eHT: Early Hesperian transition unit; IHT: late Hesperian transition unit; IHL: late Hesperian unit; Hve: Hesperian volcanic unit; AHv: Amazonian-Hesperian volcanic unit; IAv: late Amazonian volcanic unit; IHvf: Late Hesperian volcanic field unit; AHf: Amazonian and Hesperian Impact unit; Htu: Hesperian transition undivided unit; AHtu: Amazonian and Hesperian transition undivided unit. C) Gridded free-air gravity model (MRO120D (Konopliv et al., 2016)) for the landing site region with spherical harmonic degrees from 7 to 90 overlain on the MOLA hill shade. D) Magnetic field intensity map of the landing site region overlain on MOLA hill shade map following Langlais et al. (2019).

The final landing site for InSight lander (the E9 ellipse) is located in western Elysium Planitia near the dichotomy boundary, south of Elysium Mons shield volcano, in particular to satisfy the constraints on landing safety and the instrument deployment requirements (Golombek et al., 2017). Within the northern lowlands (Fig. 1), the landing ellipse is located on the flat, rocky lava plains mapped as Hesperian aged unit (eHt) (Tanaka et al., 2014). As the 4–6 km topographical difference between the northern lowlands and southern highlands formed very early (Frey et al., 2002), the dichotomy boundary has been subjected to degradation and accumulation of sediments for a large part of Mars' history. As a result of the denudation and sedimentary processes and complex volcanic history of the region, the landing site region, which includes the transition between southern highlands and northern lowlands, is geologically complex (Tanaka et al., 2014; Golombek et al., 2018), possibly with varying compositional heterogeneities and discontinuities in the subsurface. On Earth, structurally complex inhomogeneities in the subsurface affect the propagation of seismic waves, causing their reflection and diffraction (e.g. Claerbout, 1971; Schneider, 1978). For instance, shallow subsurface structures in Earth's crust generate multiple wave conversions and reverberations, which can be captured using the broad band receiver function (RF) technique (e.g. Langston, 1979; Owens et al., 1984, 1987). Recent developments (e.g. Li and Nábělek, 1999; Pham and Tkalčić, 2017; Tauzin et al., 2019) allow the extraction of pure P wave mode reverberations from single vertical component receiver functions. With these methods, the SEIS instrument onboard InSight lander including the very broad band (VBB) and short period (SP) instruments, will acquire seismic data with potential to highlight shallow subsurface structure beneath the lander.

The complex subsurface structure modifies the seismic waveforms. Depending on (an)elastic properties, weak layers buried in the subsurface may attenuate seismic signal amplitude and/or constitute efficient waveguides. Low-velocity regolith layers and sediments on top of more competent rocks could significantly increase scattering, altering seismic waveforms and complicating their interpretation (Knapmeyer-Endrun et al., 2017, 2018). In fact, both the subsurface geological structure underneath the source and the receiver introduce these modifications to seismic waveforms. This results in a significant non-uniqueness in the elastic models. The available geological information can be incorporated to achieve a more accurate and geologically interpretable solution to the seismic inverse problem (Golombek et al., 2018). Given the uncertainties of seismic data recorded at a single station on Mars, *a priori* knowledge of the bulk composition and structural discontinuities in the subsurface are crucial to correctly interpret the in-situ measurements. Observational constraints on the geologic diversity of the transition unit in the Martian dichotomy boundary are also important for the interpretation of seismic waveforms acquired by the SEIS instruments.

In this study, to better understand the regional context, compositional heterogeneities and structural discontinuities of the subsurface of southwest Elysium Planitia, we use a combination of orbital imagery and spectral datasets, including CRISM (Compact Reconnaissance Imaging Spectrometer for Mars) for mineralogy; TES (Thermal Emission Spectrometer) for thermophysical properties, HiRISE (High Resolution Imaging Science Experiment) and CTX (Context Camera) for morphology and geologic mapping. The goal of this investigation is to identify variations in the composition and physical properties of crustal materials beneath the InSight landing site region, from 125°E to 145°E, 2°S to 15°N, within ~500 km from the landing site. The regional context provides important clues to the shallow crustal structure in the first few kilometers. The geological units within this region are Noachian to Amazonian in age. To complement previous studies that investigated the geology of the InSight landing site (Golombek et al., 2017, 2018), we have focused our investigation to impact craters that reveal the structure of the crust at depth. From these observations, we construct a proposed cross-section across the dichotomy boundary, and highlight the different lithologies exposed in this region spatially and at depth. Finally, we discuss the potential implications for seismic data acquired by SEIS

instrument onboard the InSight lander based on the information of the geologic structure of the landing site region. We propose six crustal models for future modeling effort and seismic data analysis based on these geological constraints that we provide as supplementary material.

## 2. Geological and geophysical background of the landing site region

Situated between the Elysium volcanic structure and the dichotomy boundary, the InSight landing site (4.5 N, 135.9E) region has been shaped by the early formation and subsequent modification of the Martian dichotomy (Fig. 1A) (Golombek et al., 2017). In the Mars global geological map, the landing site is situated in the ridged plains unit (Hr) (Greeley and Guest, 1987), and later updated as the early Hesperian transition unit (eHt) and the late Hesperian unit (lHt) (Tanaka et al., 2014) (Fig. 1B). Subsequent detailed mapping of the InSight landing site region indicates the exposed surface unit was emplaced from Hesperian to early Amazonian based on crater counting and relations with adjacent geologic units (Warner et al., 2017; Golombek et al., 2018). At the regional scale, we refer to them (eHt, lHt) as the “Hesperian-Early Amazonian ridged plains unit”, or “ridged plains unit”. The ridged plains unit is bordered by a transition unit (HNt) to the south, younger Elysium volcanic unit (HAv) to the north, Medusae Fossae Formation (Htu, AHtu) and Cerberus volcanic unit (lAv) to the east (Fig. 1B).

Geophysical data including gravity and magnetic field measurement could provide additional information on potential subsurface heterogeneities on Mars. Based on the global Mars gravity model (MRO120D) (Konopliv et al., 2016), the gravity field of the landing site region is calculated by the summation of harmonic degrees from 7 to 90 to eliminate long-wavelength variations induced by Tharsis (Zharkov and Gudkova, 2016) (Fig. 1C). One region along the dichotomy south of the InSight landing site shows a positive gravity anomaly, which has been attributed to localized thinning of the crust from edge-driven mantle convection induced by earlier large basin-forming impacts (Kiefer, 2005). The landing site region is also marked by weak to moderate surface magnetic field anomalies, predicted by a recent model (Langlais et al., 2019) (Fig. 1D). Notably, three zones of magnetic field anomalies exceed 1000 nT, including one region northwest of the lander between the transition unit (HNt) and the ridged plains unit (eHt), and two others are located at the north and west of the Medusa Fossae Formation.

The ridged plains unit is interpreted to be underlain by lava flows, due to the existence of rocks in the ejecta of craters tens of meters to hundreds of meters in diameter, lobate lava flow fronts, platy and ridged surface textures, lava inflation plateaus, volcanic vents and the presence of wrinkle ridges (Warner et al., 2017; Golombek et al., 2018). Within the landing ellipse, the surface of the landing site is covered by >3 m thick regolith suggested by the onset diameter of rocky ejecta craters (Warner et al., 2017). A cross-section exposed at Hephaestus Fossae in nearby Utopia Planitia has been proposed to be a potential analog for the shallow structure of the unit within the landing ellipse, with a relatively fine-grained, impact-generated regolith layer that grades into coarse ejecta that overlies fractured/jointed lava flows (Warner et al., 2017; Golombek et al., 2018). This stratigraphy has been used to construct a shallow crustal structure model for the project with progressively increasing seismic and elastic properties based on focused laboratory and field investigations for better understanding seismic wave propagation in the shallow subsurface (e.g., Knapmeyer-Endrun et al., 2017, 2018; Kedar et al., 2017; Morgan et al., 2018)

To the north of this ridged plains unit is the Hesperian-Amazonian Elysium volcanic unit (HAv) (Fig. 1B). The Elysium Mons shield volcano is the third highest volcano on Mars with 12.6 km of relief (Plescia, 2004), and is covering the second-largest volcanic province on Mars (after Tharsis). Elysium Mons probably has been continuously active since 3.4–3.9 Ga until quite recently, with a peak of emplacement around 2.2 Ga (Platz and Michael, 2011; Pasckert et al., 2012). This volcanic construct created a positive gravity load on the regional

lithosphere, consistent with high-density volcanic materials (Belleguic et al., 2005; Baratoux et al., 2014; Broquet and Wieczorek, 2018). Most of the Elysium volcanic unit (HAV) is devoid of significant magnetic fields (Fig. 1D). The central Elysium region has had volcanic activity from ~300 Ma to ~2 Ma and is one of the most recently active volcanic regions on Mars (Berman and Hartmann, 2002; Vaucher et al., 2009; Hauber et al., 2011). The youngest lava flows, labeled as the Cerberus volcanic unit (IAV) (Fig. 1B) are located to the east of the landing ellipse. These Amazonian lava flows emanated from Cerberus Fossae and that flowed down Athabasca Valles (Vaucher et al., 2009; Kerber and Head, 2010). Flows from it have almost no impact craters and clearly embays the adjacent Elysium and Medusae Fossae units, and is dated at 2.5 Ma (Tanaka et al., 2014; Golombek et al., 2017, 2018; Vaucher et al., 2009).

Medusae Fossae Formation (MFF) is a morphologically unique unit in the lowlands ~210 km to the east of the landing ellipse (e.g. Malin, 1979; Scott and Tanaka, 1982). Medusae Fossae Formation is a widespread deposit with a distribution of  $2.1\text{--}2.6 \times 10^6 \text{ km}^2$  (Scott and Tanaka, 1982; Tanaka, 2000; Bradley, 2002; Hynes, 2003). MFF outliers in the subsurface have been identified with additional reflectors beneath the lava flows using orbital SHARAD (SHARAD) sounding data (Morgan et al., 2015). MFF is characterized by wind-etched surface morphology and dissected, often yardang-forming units, with distinct physical properties from nearby Martian surface with low thermal inertia, muted radar reflectivity and low density from gravity and topography data (Edgett and Malin, 2000; Hynes, 2003; Watters et al., 2007; Carter et al., 2009; Zimelman and Griffin, 2010; Ojha and Lewis, 2018). The bulk of the MFF has a surface age of Early Amazonian (Scott and Tanaka, 1982, 1986; Greeley and Guest, 1987; Hynes, 2003; Platz et al., 2013) but the lower member could be as old as Hesperian (3.8–3.0 Ga) (Kerber and Head, 2010; Zimelman and Scheidt, 2012).

To the south of the landing ellipse is a complex transition into the southern highlands, including numerous mesas, buttes, and local channels and fans (Tanaka et al., 2005, 2014). The transition unit grades into the southern highlands where 500 km-long networks of valleys exist connecting Herschel crater to Gale, Knobel and Sharp craters near the dichotomy. Notably, past aqueous activity has been identified from orbit and explored by Mars Science Laboratory (MSL) in Gale crater (Grotzinger et al., 2015). Ancient sedimentary units similar to those exposed in the adjacent highlands likely extend into the subsurface of the transition unit but are currently obscured by later volcanic flows and sediments. The widespread resurfacing events experienced in this region (Irwin et al., 2004) indicate fluvial erosion and aeolian fretting, which may result in a complex subsurface structure. We also investigate the transition unit in this study focusing on the limited exposures in craters and local scarps.

### 3. Method

#### 3.1. Investigation of the subsurface materials using impact craters

Western Elysium Planitia, where InSight landed, is covered with lava flows. This region also has a relatively high dust cover (DCI of 0.94) (Ruff and Christensen, 2002) and albedo (Golombek et al., 2017) so that surface mineralogy is likely masked. Because impact craters provide natural windows into the subsurface, we investigate the mineralogy, morphology and thermal properties of the central peaks in the landing site region through the analysis of orbital image datasets (see Section 3.2) to understand the structure of the subsurface.

##### 3.1.1. Impact excavation depth calculations

Impact craters that expose subsurface materials on their crater rims or crater floors indicate the materials are excavated from beneath the surface, within the maximum depth of excavation of the crater. The excavation depth of the impact craters is directly related to the impact energy, so the original depth of exposed materials in impact craters can be estimated based on scaling relationships to impact diameter. The

maximum depth of excavation scales with  $\sim 1/10$  of the diameter of the transient crater ( $D_{tr}$ ) (e.g. Melosh, 1989):  $d = 1/10 \cdot D_{tr}$ . The transient diameter can be expressed as a function of the crater's final diameter  $D_{final}$  using different scaling laws (Melosh, 1989; Holsapple, 1993; Croft, 1985). These scaling laws are to first-order consistent, although Croft (1985) ( $D_{tr} = D_{final}^{0.85} \cdot D_*^{0.15}$ ) predicts larger transient diameters for given final crater diameters than the other two for impact craters with  $D_{final} < 350 \text{ km}$  (Ernst et al., 2010). Here we use the scaling law derived by Holsapple (1993),  $D_{tr} = 0.758 \cdot D_{final}^{0.921} \cdot D_*^{0.079}$ , which applies for both simple and complex craters. We use 8 km as the transition diameter ( $D_*$ ) between simple and complex craters on Mars (Garvin et al., 2003).

Central peaks of larger complex craters can also be used to constrain the original depth of exposed materials. Because central peaks are formed by uplifted materials beneath the melt zone, the depth of origin can be estimated by the maximum melting depth of the impact (Grieve and Cintala, 1992; Ernst et al., 2010). Both analytical solutions based on energy balance and more complex hydrocode simulations provide comparable results with measurements of melt volumes associated with terrestrial impact craters (Pierazzo et al., 1997; Ernst et al., 2010; Abramov et al., 2012). An alternative method is to locate the original depth with terrestrial empirical relationships (Grieve and Pilkington, 1996), but the varying gravity acceleration, impactor velocity, and possible target material properties may result in discrepancies when these relationships are applied to Mars (Grieve and Cintala, 1997). Here we report calculated values from both methods. For the maximum melting depth, we use the equation derived from Abramov et al. (2012) to calculate the melt volume based on the energy balance (Bjorkman and Holsapple, 1987):

$$V_{melt} = 0.12 E_m^{-0.85} \left( \frac{\rho_p}{\rho_t} \right)^{-0.28} D_{tc}^{3.85} g^{0.85} \sin^{1.3} \theta \quad (1)$$

Here the  $E_m$  is the specific energy of the target of the Rankine–Hugoniot state from which the isentropic release ends at the 1-bar point on the liquidus (Bjorkman and Holsapple, 1987);  $\rho_p$  and  $\rho_t$  are densities of the projectile and target, respectively;  $D_{tc}$  is the transient cavity diameter,  $g$  is the surface gravity acceleration,  $\theta$  is the impact angle. The transient cavity diameter is calculated as  $D_{tc} = \frac{D_{tr}}{1.2}$  (Pike, 1977) where  $D_{tr}$  is the transient crater diameter, determined using two different scaling relationships (Croft, 1985; Holsapple, 1993). The maximum melting depth is approximated as the diameter of a spherical melt region (Pierazzo et al., 1997; Abramov et al., 2012), so:

$$d_m = 2 \left( \frac{3}{4\pi} V_{melt} \right)^{\frac{1}{3}} \quad (2)$$

The values of different variables are chosen for Mars based on those used in the literature, as referenced in Table 1.

We also calculate the structural uplift based on empirical scaling of terrestrial craters (Grieve and Pilkington, 1996):

$$SU = 0.086 D^{1.03} \quad (3)$$

The calculated original depth based on maximum melting depth is broadly consistent with the empirical scaling law with differences  $< 0.3 \text{ km}$  for impact craters with diameters smaller than 100 km. Given the uncertainties of target property and physical parameters of the impactor, we use this calculation only as a first-order estimate. With the original depth of the central peak materials, we can then construct the relationship of the subsurface structures based on the mineralogy and physical properties of the materials exposed in the central peak.

##### 3.1.2. Modified and buried impact craters

Empirical relationships allow determining the depth and rim height of pristine impact craters from the diameter of an impact crater. Comparing theoretical values with observed depths and rim heights indicate if observed impact craters are partially buried or modified by

**Table 1**  
Variables used in the maximum melting depth calculation.

Variable	Definition	Values	Dimension	References/ comments
$E_m$	Specific energy of the target upon pressure release	$9 \times 10^6$	J/kg	For dunite <sup>a</sup> (Pierazzo et al., 1997)
$\rho_p$	Density of projectile material	3350	kg/m <sup>3</sup>	The typical density of ordinary chondrite
$\rho_t$	Density of target material	2900	kg/m <sup>3</sup>	The typical density of basalt
$g$	Gravity acceleration	3.7	m/s <sup>2</sup>	Gravitational acceleration for Mars
$\theta$	Impact angle	0.785	rad	45°, a most probable angle of impact

<sup>a</sup> Dunite is the closest match (among metal, ice, granite) to possible mafic mineralogy with validated melt calculations (Pierazzo et al., 1997; Barr and Citron, 2011). Although a basaltic target would indicate greater melting depth than a dunite target, the difference is expected to be smaller than 21%, based on the parameters for granite.

the emplacement of a second unit (e.g., lava flow or sediments). Hence, the observed morphology of impact craters can be used to constrain the thickness of overlying layers. Here we map buried and modified impact craters (>3 km) in the landing ellipse vicinity based on orbital imagery as well as topography dataset to better constrain the thickness of the lava flow unit.

For identification of buried and modified impact craters, we use global datasets including gridded global topographic data from MOLA (Mars Orbiter Laser Altimeter) instrument (Smith et al., 1999; Zuber et al., 2000), global imagery from THEMIS day-time infrared global mosaic at 100 m/pixel resolution (Edwards et al., 2011), and CTX mosaic at 6 m/pixel (Dickson et al., 2018). For the measurement of impact crater morphometry (including depth, diameter, and rim height), we create a Digital Terrain Model (DTM) using CTX stereo pairs covering the impact crater using the Ames Stereo Pipeline (Beyer et al., 2018). We use the HRSC DTM (where the elevation postings are at 75 m) and MOLA gridded elevations (128 pixels/deg) in the case of two complex craters with no CTX stereo pair coverage, but with diameters (>15 km) large enough to be well-resolved using MOLA PEDR and HRSC datasets. For a given impact crater, we measure the elevation of the crater rim, crater floor and the region outside 1 radius of the impact crater by taking the average of 5–6 hand-picked sample points for each measurement. The averaged elevations of the crater rim ( $H_r$ ), floor ( $H_f$ ) and outside region ( $H_o$ ) are then used to compute the crater depth ( $d = H_r - H_f$ ) and crater rim height ( $r_h = H_r - H_o$ ) (Robbins and Hynek, 2012).

To estimate the original morphometry of impact craters, we utilize the crater statistics of fresh impacts. For Mars, the impact crater morphometry and relationships with diameter have been investigated by Stewart and Valiant, 2006; Boyce and Garbeil, 2007; Robbins and Hynek, 2012; Tornabene et al., 2018. The northern lowlands' impact craters are significantly deeper (as much as 1.5–2.0 times deeper for simple craters (Stewart and Valiant, 2006)). Here we calculate the original rim height and depth of buried or modified impact craters based on the statistics of fresh impact craters in Isidis basin (Stewart and Valiant, 2006) with likely similar target property as Elysium. The scaling relationships for depth  $d$  and rim height  $r_h$  as a function of diameter  $D$  are given by:

$$d(D) = 0.213 D^{1.02} \text{ (Simple craters)} \quad (4)$$

$$d(D) = 0.494 D^{0.43} \text{ (Complex craters)} \quad (5)$$

$$r_h(D) = 0.036 D^{1.03} \text{ (Simple craters)} \quad (6)$$

$$r_h(D) = 0.133 D^{0.51} \text{ (Complex craters)} \quad (7)$$

The classification of impact craters (simple or complex craters) is determined considering the impact crater diameter as well as its morphological features. The calculated original depth and rim heights of impact craters are then compared to the measured depth and rim heights to compute the thicknesses of the overlying unit.

### 3.2. Image datasets

We use both spectral and high-resolution imagery to understand the mineralogy, morphology and measure features of individual geologic units.

#### 3.2.1. Hyperspectral observation from CRISM

CRISM (Compact Reconnaissance Imaging Spectrometer) is a hyperspectral imaging spectrometer that acquires hyperspectral data in the visible to near-infrared wavelength region (Murchie et al., 2007). These data can be used to understand the composition and mineralogy of the martian surface (Murchie et al., 2009). In this study, we processed 89 CRISM (Compact Reconnaissance Imaging Spectrometer for Mars) targeted images for L-detector (438 channels covering wavelength range of 1–4  $\mu\text{m}$ , with a spatial resolution of 18–36 m/pixel) in the landing site region (125°E to 145°E, 2°S to 15°N). We download the I/F data from Planetary Data System and then process the datasets following the data processing method detailed in the CRISM image survey of the northern lowlands of Pan et al. (2017). In this processing, we perform atmospheric and geometric corrections using the CRISM Analysis Toolkit and remove spikes and spurious pixels in the image cube. We then calculate the spectral ratio of each pixel in the image to the median spectrum of pixels without particular spectral features in the same column. The ratioed cube shows enhanced spectral absorption features and is later used to compute a spectral parameter map that highlights these spectrally distinct regions. The scene-wide ratio depends on the dominant mineralogy of the scene and may confound spectral identifications when the denominator consists of broad spectral features (e.g. in mafic minerals), so this is mostly applicable to images where most regions are spectrally bland. Therefore, we use these new products (ratioed image and spectral parameters) in addition to the original spectra of the region of interest to identify locations with distinct mineralogy from the rest of the image. We also use canonical spectral parameters (Viviano-Beck et al., 2014) to validate the denoised products and make spectral parameter maps.

#### 3.2.2. Imagery from HiRISE and CTX

We analyze HiRISE (High Resolution Imaging Science Experiment) and CTX (Context Camera) images covering impact crater central peaks in the study region and the transition unit between the lowlands and highlands, in order to further investigate the correlation of the CRISM mineral detections with morphological units. The HiRISE instrument (McEwen et al., 2007) onboard Mars Reconnaissance Orbiter (MRO) is a camera taking high-resolution images in the visible spectral domain with a spatial resolution up to 25 cm/pixel. The CTX instrument is another imager onboard MRO (Malin et al., 2007; Bell et al., 2013) that now offers 97.3% coverage of Mars with a spatial resolution of  $\sim 6$  m/pixel (Dickson et al., 2018). We investigate the central peaks of impact craters in the study region when HiRISE coverage exists; when absent, we utilize CTX images. Both HiRISE and CTX images are downloaded, calibrated and projected using the United States Geological Survey (USGS) Integrated Software for Imagers and Spectrometers version 3 (ISIS3) software (e.g. Becker et al., 2013) enabled on the MarsSI data processing platform (Quantin-Nataf et al., 2018). To resolve the fine layering and measure the thickness of layers exposed in Kalpin crater, a stereo Digital Elevation Model (DEM) was made using Planetary Data System (PDS) HiRISE (McEwen et al., 2007) Experimental Data Records (EDRs) and standard methods (e.g. Kirk, 2003; Kirk et al., 2008). The data are first pre-processed in the Integrated Software for Imagers and Spectrometers (ISIS), before importing into SOCET SET, available from

BAE Systems, to produce DTMs and ortho-rectified images, and final post-processing in ISIS. We estimate the vertical precision of the DTM as 0.2 m, by assuming 1/5-pixel correlations during processing (Kirk et al., 2008; Okubo, 2010). We measure the orientation and dip of the layers using the LayerTool add-in to ArcGIS (Kneissl et al., 2010) and calculate the layer thicknesses based on topography and layer dips.

## 4. Results

### 4.1. Mineralogy survey of the landing site region

Eighty-nine CRISM targeted images were analyzed covering the study region (125–144° E, –2–15° N) and are listed in Appendix A. Due to the limited outcropping surfaces, CRISM images unrelated to impact craters are mostly dominated by the spectral feature of dust or regolith, masking the mineralogy of the bulk geologic unit, consistent with previous global studies of Mars' surface using OMEGA data (Ody et al., 2013). Despite the effect of the dust cover, we have identified phyllosilicates, olivine and low-calcium pyroxene (Fig. 2) based on their specific spectral features in the near-infrared wavelength region, following the method given in Section 3.2.1. Here we discuss in detail the spectral features identified, their distribution and relationship with geologic features in this region.

#### 4.1.1. Mafic detections in the volcanic units

Olivine is identified based on the complex absorption at 1.0  $\mu\text{m}$ , a combination of several broad bands due to  $\text{Fe}^{2+}$  orbital splitting (Burns, 1993). Depending on the composition of the olivine mineral and grain size, the relative strength of the absorptions would vary due to different orbital splitting and volumetric scattering (Sunshine and Pieters, 1998; Clénet et al., 2011). The spectral signature of olivine is identified in CRISM targeted images to be widespread (Fig. 2), within the ridged plains unit (eHt, lHt), the transition unit (HNt), as well as the Elysium volcanic unit (AHv). No detections have been identified in the Cerberus Fossae unit (lAv) and the Medusae Fossae Formation (Htu, AHtu). The

widespread olivine detections are consistent with previous findings (Ody et al., 2013; Pan et al., 2017). Within the smooth plains unit adjacent to the InSight landing site, weak absorptions ( $\sim 1\%$ ) around 1.0  $\mu\text{m}$  consistent with olivine spectral features in ratioed CRISM spectra (Fig. 3) have been identified. These signatures are detected on small crater rims close to the landing site, mostly in the ridged plains unit (Fig. 3).

In two of the small impact craters in the late-Hesperian ridged plains unit (lHt) (Tanaka et al., 2014) (FRT00009591, FRT00008330), we identify spectra with broad absorptions at both  $\sim 1 \mu\text{m}$  and  $\sim 2 \mu\text{m}$ , distinct from the olivine spectra. The absorption band depth is small, as with the olivine spectra, but the bandwidths and positions are consistent with the near-infrared spectra of pyroxene, which are characterized by the broad absorption features at  $\sim 1.0 \mu\text{m}$  and  $\sim 2.0 \mu\text{m}$  (Hazen et al., 1978; Burns, 1993). Both absorption bands occur at shorter wavelengths for low-calcium pyroxene (LCP) (0.92–1  $\mu\text{m}$  and 1.85–2.15  $\mu\text{m}$ ) than high-calcium pyroxene (1–1.04  $\mu\text{m}$  and 2.0–2.25  $\mu\text{m}$ ) (Hazen et al., 1978). The location of the 2  $\mu\text{m}$  band in these images is in between the two suggested endmembers, close to low-calcium pyroxene (LCP).

#### 4.1.2. Fe/Mg phyllosilicate detections in Kalpin crater and the transition unit

Fe/Mg phyllosilicate is the most widespread hydrated mineral found on Mars (Ehlmann et al., 2011; Carter et al., 2013; Ehlmann and Edwards, 2014). They are characterized by the distinctive, sharp absorption bands at 1.39–1.41  $\mu\text{m}$ , 1.91  $\mu\text{m}$  and 2.28–2.31  $\mu\text{m}$  due to the vibrations of metal-OH bond within the octahedral layer and molecular  $\text{H}_2\text{O}$  in the interlayers of the phyllosilicates. In the InSight landing site region, we have identified phyllosilicates in two locations, in the Elysium volcanic unit and the transition unit southwest of the landing site (Fig. 2).

We have identified phyllosilicates in the 51-km Kalpin crater (8.93°N, 141.27°E) on the southwest flank of Elysium Mons north of the landing site (Figs. 2, 4), consistent with previous work (Carter et al., 2013; Sun and Milliken, 2015; Turner et al., 2016; Pan et al., 2017).

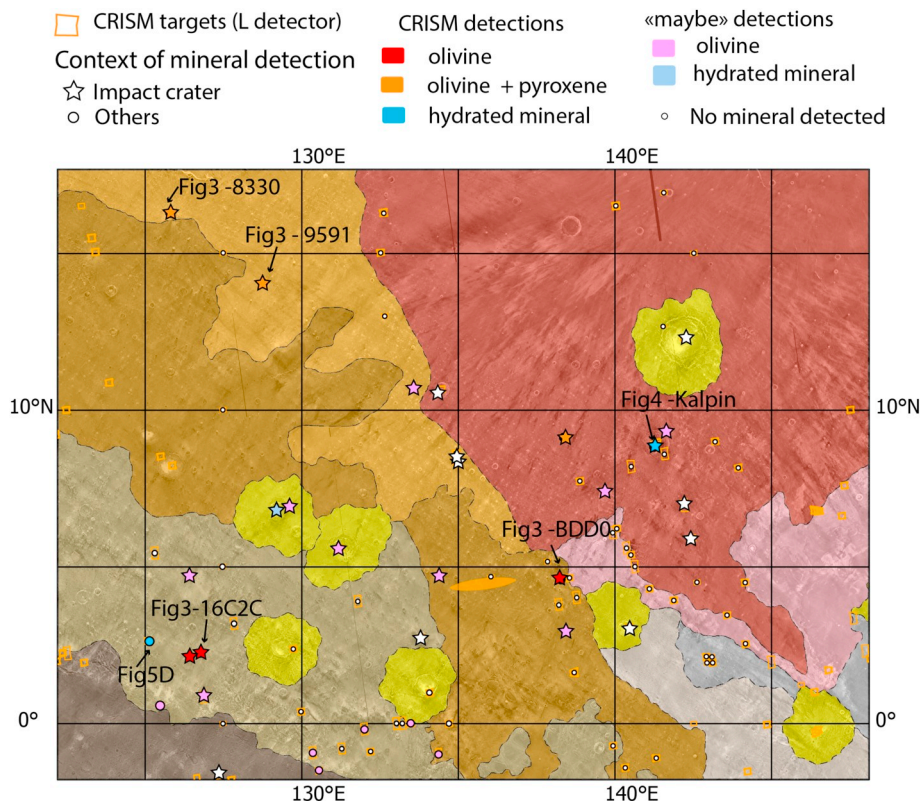


**Fig. 2.** Mineralogy mapping of the landing site region (InSight ellipse shown in orange). CRISM targeted images with L-detector data are shown on this map region. Targets with symbols denote the CRISM images investigated in this study, with the identified mineralogy indicated by the color of the symbols. Stars indicate images covering part of or all of an impact crater with diameter larger than 1.5 km, and circles indicate CRISM images covering other types of geological features. Impact craters shown in Fig. 3 and Fig. 4 are indicated with arrows. The base map is THEMIS nighttime infrared mosaic overlain by the geologic map units from Tanaka et al. (2014) (Fig. 1B) in Mars equirectangular projection.

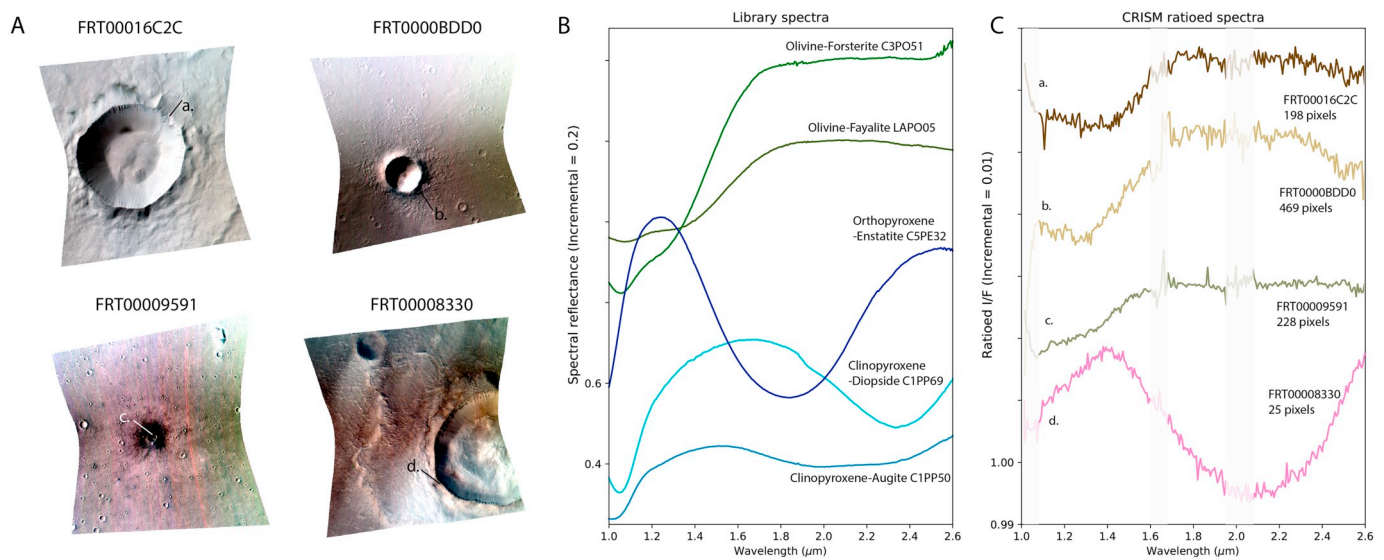


**Fig. 3.** Mafic mineral detections in the landing site region exposed from 4 small craters with diameter 1.5–7 km in CRISM targeted images. Locations of these images are shown in Fig. 2 denoted by the image ID. Type examples of craters shown are from the transition unit (FRT0016C2C) and the ridged plains unit (FRT0000BDD0, FRT00009591, FRT00008330). A. CRISM false-color images of the three example images, with short lines pointing to the regions of interest where the numerator of CRISM ratioed spectra in 3C are acquired. B. Library spectra from the CRISM spectral library of olivine and pyroxene. C. CRISM ratioed spectra of mafic mineral detections in small impact craters. Instrumental artifacts near 1  $\mu\text{m}$ , around  $\sim 1.65 \mu\text{m}$  and atmospheric residuals at  $\sim 2 \mu\text{m}$  have been masked with semi-transparent layer. The number of pixels used to obtain the average spectra is given beneath the image IDs.

Spectral absorptions occur at 1.91 and 2.30  $\mu\text{m}$ , with a weak 1.4  $\mu\text{m}$  absorption. The band position at 2.30  $\mu\text{m}$  lies in between the Fe and Mg-endmembers of Fe/Mg phyllosilicates (2.28–2.31  $\mu\text{m}$ ) and does not allow for distinguishing between different types of Fe/Mg phyllosilicate. The pixels with the strongest absorption features of Fe/Mg phyllosilicates are correlated with a low-albedo, fractured unit adjacent to the central peak, while the bulk of the central peak does not have these features. Other than in Kalpin crater, phyllosilicates have only been detected in the transition unit southwest of the landing site. (Figs. 2, 5). Here phyllosilicate detections are correlated with the upper part of the knobs and ridges in a chaotic terrain (Fig. 5).

#### 4.2. Morphology and distribution of the layered deposits in the landing site region

To understand the distribution and diversity of materials in the study region, we analyzed images covering the central peaks and crater walls of well-preserved complex craters and exposed crater walls of simple craters (Appendix B). Thirty-five fresh impact craters with diameters from 4 to 84 km have been identified in HiRISE and/or CTX coverage (Fig. 6), of which twenty-six impact craters are complex craters with a prominent central structure. We have found six craters (including Kalpin crater) that exhibit outcrops in the center peak or on the crater floor with distinct yardangs (Figs. 6–7). These outcrops show extensive layering in HiRISE images (e.g. Fig. 8). Although the layers cannot be well resolved in CTX images resolution ( $\sim 6 \text{ m/pix}$ ), but the erosional morphology of the deposit can be recognized. The six impact craters that exposed layered outcrops have diameters ranging from 13 to 51 km (Fig. 7A–F), and are clustered in a region north of the Medusae Fossae Formation, northeast to the InSight landing site (Fig. 6). The size of the exposed layered outcrops varies from 1.8  $\text{km}^2$  to 131.9  $\text{km}^2$ . In these impact craters, the layered deposit is commonly found adjacent to the central peak (e.g. Fig. 7A–C, E–F), but in one small complex crater they are found near the crater rim (e.g. Fig. 7D). The offset to the center of the crater is not correlated with crater size or distance to the Medusae Fossae Formation.

Kalpin crater is the largest crater that exposes this unit. The bulk of the central peak of Kalpin crater consists of a fragmented, knobby unit

characterized by relatively light-toned materials with heavily eroded morphology (Fig. 8). The alternating resistant (cliff-forming) and friable (slope-forming) layers in this unit form an irregular cliff-bench morphology, exhibiting extensive layering in HiRISE resolution (Fig. 8A–B). The layered structure can be distinguished in the HiRISE images at full resolution (Fig. 8). In Kalpin crater, measured thicknesses of the layers based on a HiRISE DEM are found to be 2–5 m or thinner.

We map the layer orientation and dip in the HiRISE DEM within Kalpin crater central peak at six locations. Although the layers are widespread in this unit, continuous and well-exposed layers are rare. The layers dip at varying angles from  $\sim 4$  to  $15^\circ$  in a variety of orientations (Fig. 8C). No systematic trend of the orientation or dip with the spatial location of the outcrop is observed. Extensive fragmentation is observed in this unit on relatively flat surfaces that are exposed from sand and dust cover, where HiRISE image is available (Fig. 9). Flat surfaces of the deposits exposed in HiRISE images show fracture networks. Fractures are mapped as dark-toned linear segments inside light-toned sediments, typically 1–2 pixels wide, indicating a width of  $< 50 \text{ cm}$ . Most segments are straight rather than arcuate or curvilinear and some could be traced continuously for 100 m. No obvious fillings or raised ridges are observed along the cracks, except possible dark sands. Near steep slopes, large decameter-sized blocks are shed off the edge, following pre-existing fractures (Fig. 9D, H). The fractures form along preferential directions at around 45, 90, 135 degrees (Fig. 9E–H) in Kalpin and Wafra craters.

#### 4.3. Sedimentary units of the transition unit

HiRISE images covering the transition unit between the highlands and the ridged plains unit have been surveyed in order to understand the material in contact with the lava flows. Owing to the proximity of the InSight and Curiosity landing sites, this region has less HiRISE coverage due to preferential targeting at landing sites during shared orbits. The transition unit consists of eroded mesas and mounds of unknown origin (Tanaka et al., 2014) that are embayed by later lava flows. In other locations, we identify meter-scale layering (e.g. Fig. 10A–B, D, G), yardang-forming units (e.g. Fig. 10A, E) scattered in the transition unit.

An area with clustered small impact craters is found on a small

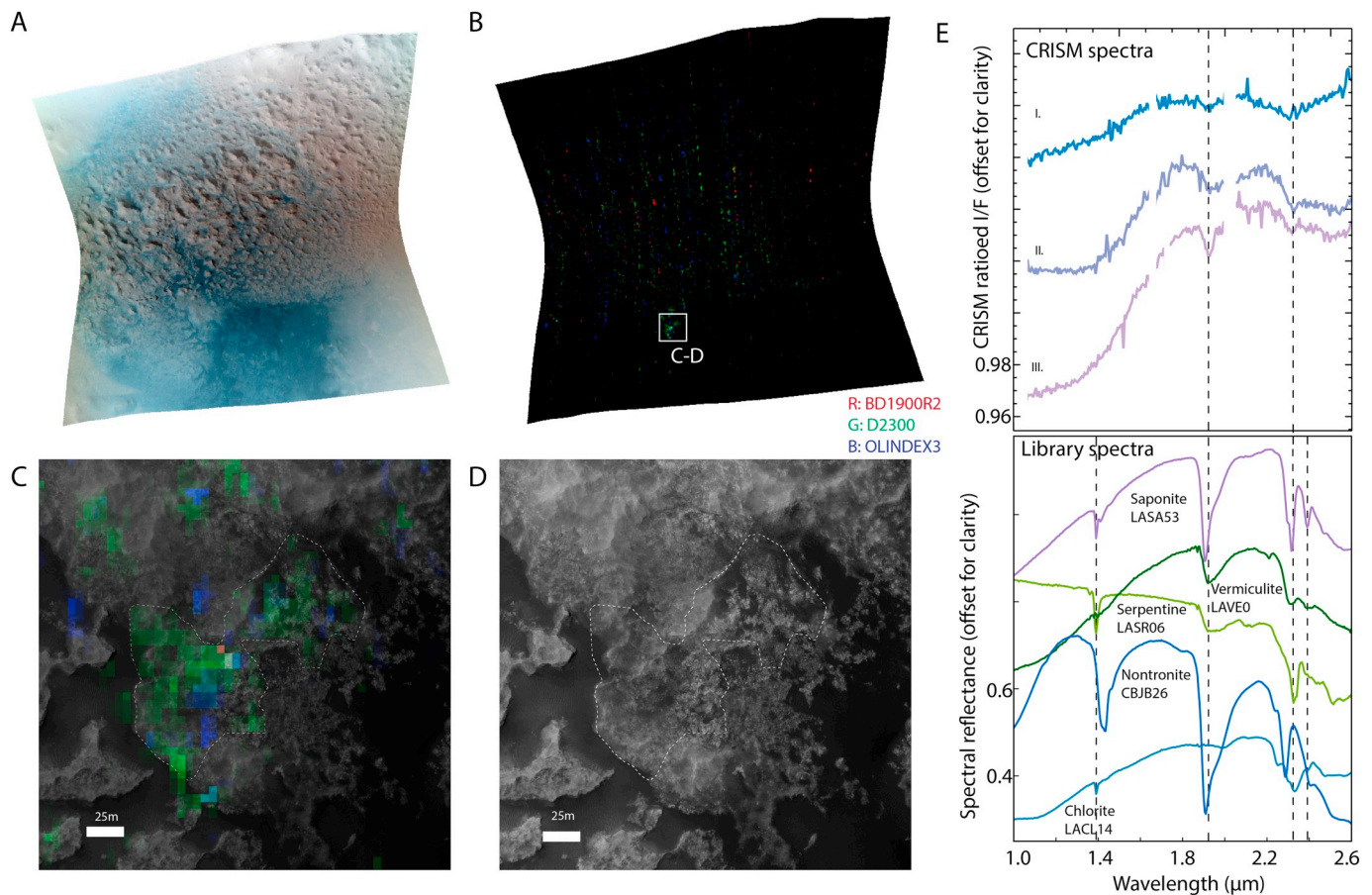


**Fig. 4.** Phyllosilicate and hydrated mineral found in the Kalpin impact crater north of the landing site in the Elysium volcanic unit. The geologic context is given in Fig. 2. A. CRISM visible false-color image FRT0000619D (R: 592 nm G: 534 nm B: 494 nm) with arrows pointing to the locations of Fe/Mg phyllosilicates (purple) and probable detections (blue). B. CRISM spectral parameter map (Viviano-Beck et al., 2014) showing the band depths of 1.9  $\mu\text{m}$  (Red), 2.3  $\mu\text{m}$  (Green) and broad absorption at 1.0  $\mu\text{m}$  (Blue), highlighting phyllosilicate detections in bright colors. The white box outlines the region of C-D. C. CRISM parameter map overlain on the HiRISE image ESP\_043051\_1890 with white dotted line showing the area of the strongest CRISM absorption bands. D. The texture of phyllosilicate-bearing deposit in HiRISE image ESP\_043051\_1890. The extent and the white dotted lines are the same extents as in C. E. Type spectra of phyllosilicate detections compared with the library spectra of typical phyllosilicates with a 2.3  $\mu\text{m}$  absorption feature. Instrumental artifacts and atmospheric correction residuals are masked for the CRISM data. (For interpretation of the references to color in this figure legend, the reader is referred to the web version of this article.)

mound in HiRISE image PSP\_008648\_1810 (Fig. 10C). Most of these small craters with a diameter around 2–10 m shows non-circular light-toned ejecta blanket that covers >1–3 crater radii. The morphological features and distribution of small impacts here suggest their formation as secondary craters with reduced impact energy. Similar bright ejecta small craters found near the InSight landing site have been identified as secondary craters from Corinto impact (Golombek et al., 2017). Many embedded craters (100–300 m in diameter) in this region indicates that this sedimentary unit is at least 10–30 m thick, and likely more and that some units are easy to erode. In a small region on the same mound, where part of the overlying layer has been eroded, irregularly spaced ridge features (2–4 m in width) have been identified (Fig. 10F). The distribution and outcrop are not as extensive as Medusae Fossae formation, but the physical properties are similar suggesting a sedimentary origin. From the existing dataset, we are unable to identify their relationship to any volcanic deposit within the unit. It is likely that the transition zone is complex, with repeated layering of aeolian sediments, fluvial sediments, and volcanics, a global characteristic of the dichotomy transition region.

#### 4.4. Extent and thickness of the lava flow unit

In the study region, the surface expressions of small craters indicate that they have been partially filled by lava flows. Some craters have their

ejecta embayed by lava flows and others have been almost completely filled (Fig. 11). We analyzed the thickness of the lava flow unit by quantifying the modifications undergone by these partially and almost completely buried impact craters. We measured the diameter, depth and rim height of these craters, using topographic profiles based on the computed Digital Terrain Models (see Method Section 3.1), which were then compared to the original crater morphometry. All of the impact craters studied here show smooth, ridged lava plains and/or aeolian sediments on the surface, with shallow depths and distinguishable rims in topography data. Because the impact craters could have degraded by mass wasting and erosion prior to being flooded by lava, the comparison of the original, fresh morphometry with that measured in the topographic maps provides a maximum estimate of the thickness of the lava flow unit. We estimate the depth of the lava flows near the landing site to be 0.16–0.18 km while away from the landing site the thickness can reach 0.59–0.62 km (Table 2). Most of these buried small craters are located on the rim of the large quasi-circular depressions (Warner et al., 2017; Golombek et al., 2018) (Fig. 11A). It is possible that the overlying lava flows are thicker toward the center of these quasi-circular depressions.

#### 4.5. Excavation depths of impact craters with exhumed materials

Impact craters that expose materials from the subsurface discussed in

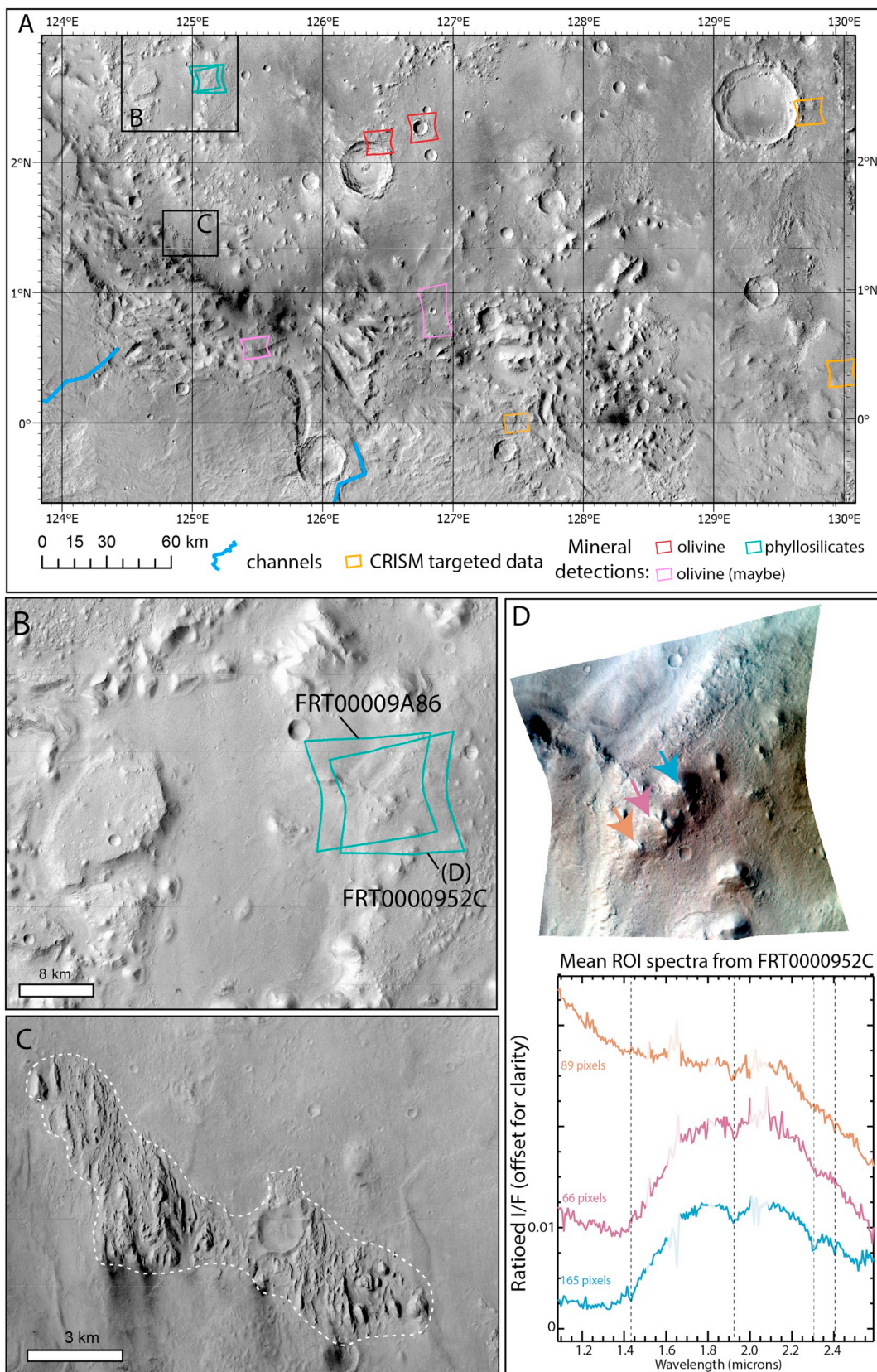


**Fig. 5.** A) Region of the transition unit near dichotomy boundary west of the InSight landing site. The background image is a CTX mosaic with CRISM targets. Blue lines highlight the location of river channels. B) Location of the phyllosilicate detection in the transition unit, giving context to Fig. 7. C) Layered, yardang-like deposits exposed near the dichotomy. D) Fe/Mg Phyllosilicate detected in the transition unit. A false-color RGB composite of the CRISM image FRT0000952C is shown, with arrows of different colors pointing to the location where the spectra are obtained and the type spectra from this CRISM image. Instrumental artifacts at  $\sim 1.65 \mu\text{m}$  and atmospheric residuals at  $\sim 2 \mu\text{m}$  have been masked with a semi-transparent layer. Dashed lines showing the observed absorption features at 1.41–3.19  $\mu\text{m}$ . (For interpretation of the references to color in this figure legend, the reader is referred to the web version of this article.)

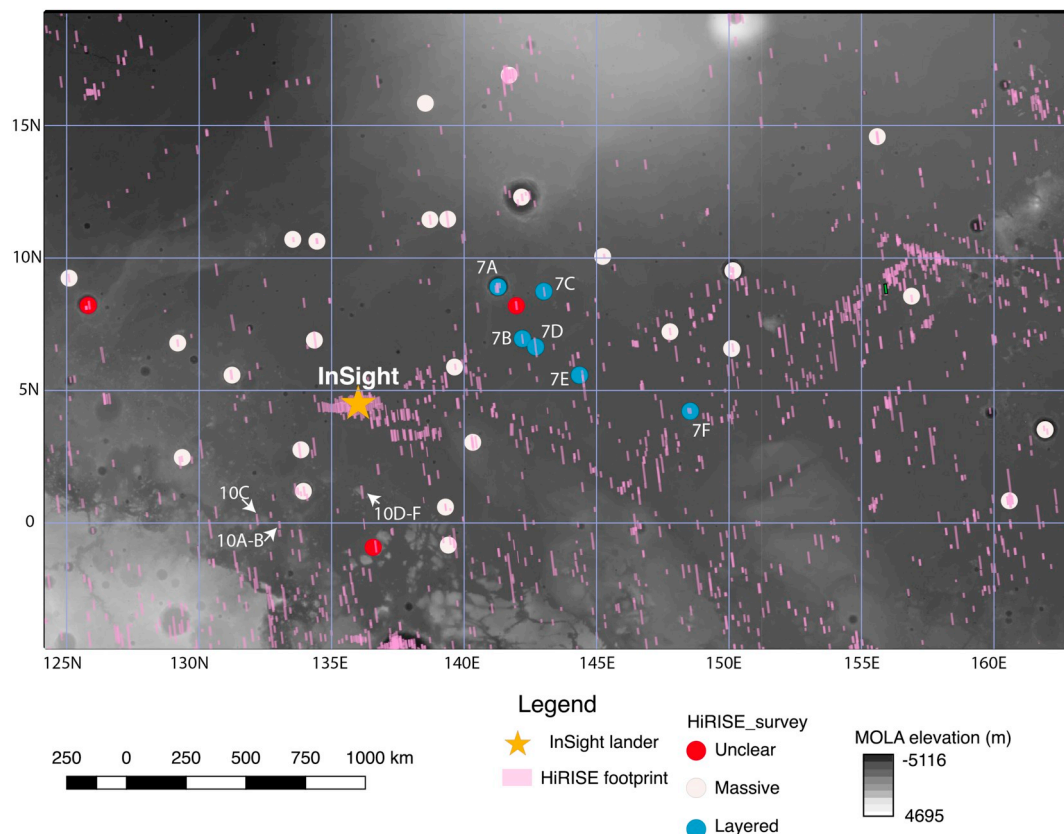


**Fig. 6.** Spatial distribution of the layered deposit identified in HiRISE and CTX image survey. Impact craters with layered deposits found on the crater floor or near the central peak are labeled 7A–7F. HiRISE images shown in Fig. 10 are highlighted by arrows. (For interpretation of the references to color in this figure legend, the reader is referred to the web version of this article.)

Sections 4.1–4.3 provide clues to the subsurface stratigraphy. Small impact craters expose olivine and pyroxene in their crater rims, while we find layered deposits and Fe/Mg phyllosilicates in larger, complex craters. We estimated the pre-impact depth of these exposure rocks (Table 3). In case of exposure in the crater rim, we calculate the maximum excavation depth. For central peak of complex craters, we calculate both the maximum melting depth and structural uplift from terrestrial empirical relationship. One complex crater exposes layered deposits on the crater floor adjacent to the central peak (Fig. 7C) and we provide calculation for the excavation depths, melting depth, and structural uplift calculations. These calculations give a first-order estimate of the relative stratigraphy in depth. Mafic minerals are exposed in craters that excavate within the first hundreds of meters (0.13–0.54 km) while Fe/Mg phyllosilicates likely originate from 5 to 6 km in depth. Layered deposits are only found in craters larger than 13 km, so if excavated, they likely originate from beneath 1 km depth.

## 5. Discussion

### 5.1. The origin of the ridged plains unit

Although mineral detections in CRISM hyperspectral data in the landing site region are not common, likely due to the dust cover (Mustard, 2005), scattered shallow subsurface outcrops over scarps and impacts have shown that the mineralogical diversity of the subsurface. The olivine signature is mostly found in the rim of small craters (diameter  $\sim$ 1.5–7 km) indicating this composition applies to the first hundreds of meters into the ridged plains units, whereas the mineralogy of the surface unit has been masked by coating or dust like over most of the northern plains materials (Mustard, 2005). However, olivine is not detected in association with large craters. This could be due to the fact

that larger craters are older so that the mineral signatures are subdued by later mantling dust. Alternatively, deeper strata could be less olivine-rich than the most recently formed layers that make up the upper 200–500 m of the stratigraphy. Although an olivine-rich signature alone may not be exclusive to volcanic lavas on Mars (Rogers et al., 2018), morphological evidence including lobate flow fronts, inflation plateaus, volcanic vents, wrinkle ridges and rocky ejecta craters, together suggest that the ridged plains unit where the InSight lander is located has a volcanic origin (Golombek et al., 2018).

### 5.2. The origin of Fe/Mg phyllosilicate in the volcanic units

Fe/Mg-phyllosilicate has been detected in the 51-km Kalpin crater (8.93°N, 141.27°E) northeast of the landing site. They are found close to the central peak, where platy, fractured, light-toned materials are exposed near dark sand dunes gathered on the crater floor. The central peak of Kalpin crater has scattered, weaker absorptions of 1.9  $\mu$ m band due to H<sub>2</sub>O and possible 2.3  $\mu$ m absorption, which suggests hydrated minerals may be present but are obscured due to higher dust component. The presence of Fe/Mg phyllosilicates indicates water-rock interactions either before or after the crater formed. The association with exposed bedrock on the crater floor and possibly on the central peak suggests their origin as excavated subsurface materials, while an alternative interpretation is they formed within a post-impact hydrothermal system (Turner et al., 2016). We find no other morphological evidence of fluvial activity in this region inside the Elysium volcanic unit, and no other hydrated mineral has been found in this unit. Given the lack of evidence of hydrothermal activities in other parts of the Elysium volcanic unit, we favor the interpretation that the phyllosilicates may have been excavated by the Kalpin impact.

Other definitive olivine and clay detections are found in the

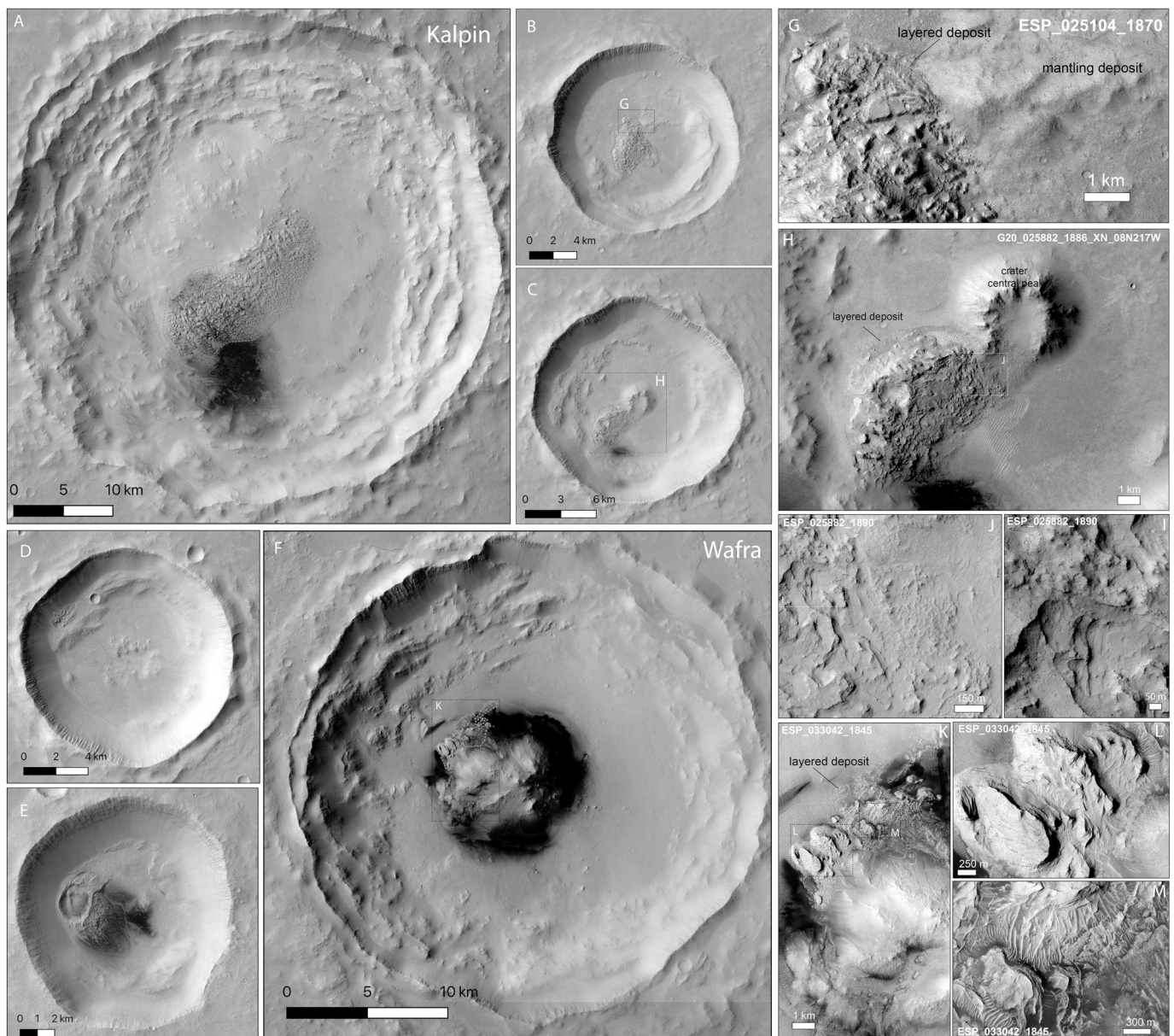


**Fig. 7.** CTX and HiRISE images over impact craters with layered deposits. A–F) CTX image or mosaic covering six impact craters with red dotted line outlining the location of layered deposits as denoted in Fig. 6. The layered deposits are found near the center of the crater, except D where they are found near the crater rim. The spatial extents of the G–M images are indicated. G. HiRISE image showing the contact between layered deposit and mantling deposit of the crater in B. H–J) CTX (H) and HiRISE (I–J) images of the central peak and layered deposit in Fig. 9C. K–M) HiRISE images showing the location and morphology of the layered features in F. CTX/HiRISE image IDs of close-in locations are labeled in Images G–M.

transition unit close to the dichotomy. Fe/Mg phyllosilicates are also reported to be widespread in the watershed of the adjacent highlands (Ehlmann and Buz, 2015) and within Gale crater (e.g. Milliken et al., 2010). The composition of the Fe/Mg phyllosilicates in the transition unit is similar to the detections on the Sharp-Knobel watershed but lacks the absorption band due to Al substitution in nontronite identified in Gale crater (Milliken et al., 2010). These findings suggest at least part of the transition unit could be the remnants of highlands materials and that there is an intrinsic connection between the transition units and the widespread, hydrated mineral-bearing sedimentary units in the adjacent highlands.

### 5.3. Possible origins of layered deposits

The central peak of the 51-km diameter Kalpin crater in the Elysium

volcanic unit shows a light-toned, cliff-bench morphology. This type of morphology has been identified in five other impact craters as small deposits on the crater floor and is consistent with the previously identified “onion skin” topography in Mars Orbiter Camera images in the Medusae Fossae Formation (Mandt et al., 2008), interpreted as aeolian erosion of layers based on terrestrial analogs. This morphology is also consistent with the attributes of sedimentary rocks identified elsewhere on Mars (Malin, 2000). We propose the layered deposits exposed in central peaks and on crater rims are likely excavated subsurface material based on several observations. First, all of the observed layered deposits occur in craters with a diameter larger than 13 km, and we have not identified such deposits in smaller craters in this region. This clear dichotomy of exposed materials in craters of different sizes is consistent with the scenario where these layered materials were exposed by impacts large enough to excavate material beneath the lava flows. Second,

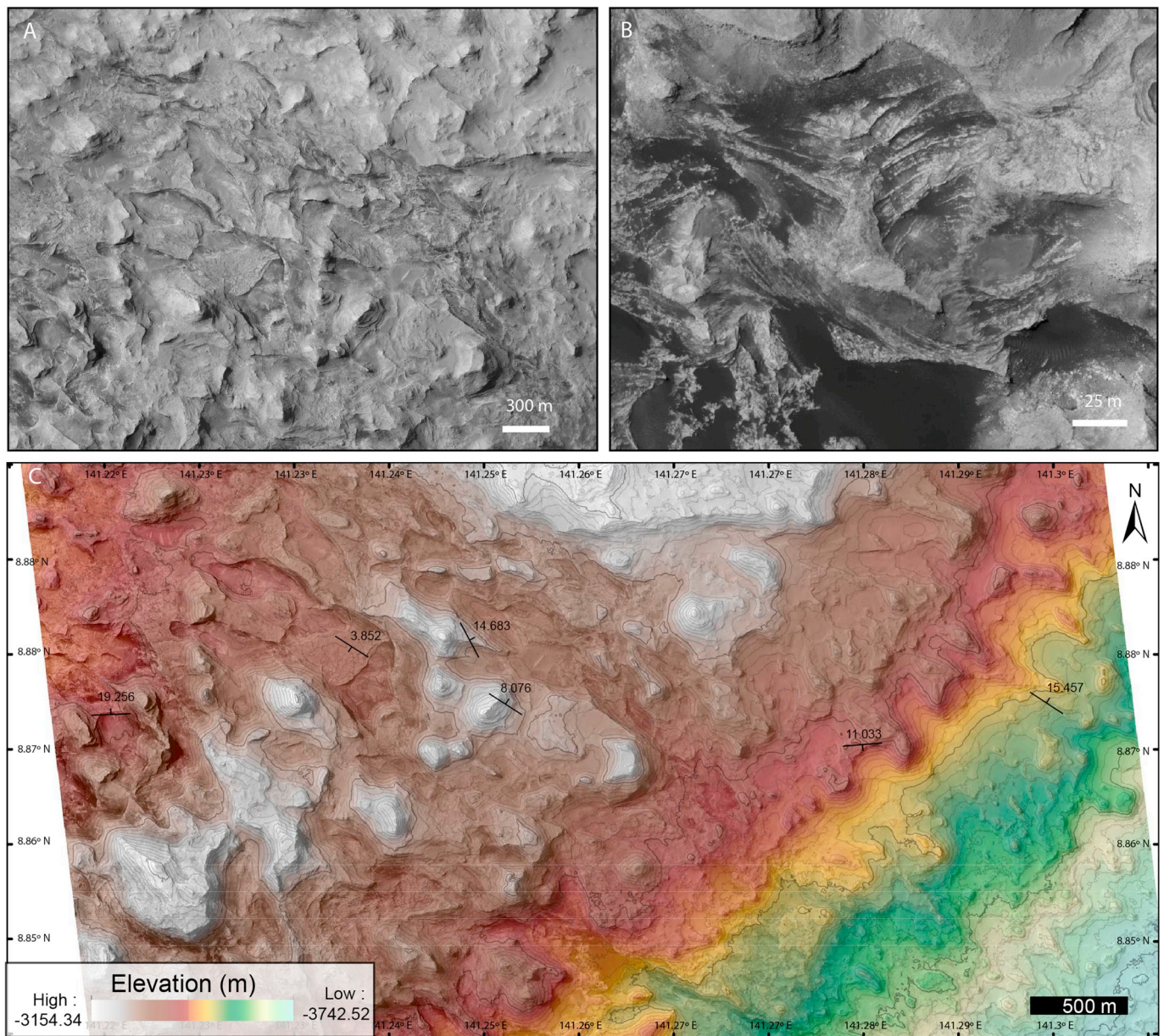


**Fig. 8.** Morphology of the central peak of Kalpin crater exhibiting features consistent with a layered structure and subject to erosion. A). The morphology of the central peak of Kalpin crater with erosional feature (HiRISE image PSP\_008305\_1890). B). The erosional features showing materials with alternating strengths (HiRISE image ESP\_043051\_1890). C). Digital elevation model of the HiRISE images (PSP\_008305\_1890 and PSP\_008806\_1890) overlying the image, with strike and dip measurement in 6 locations where layers are well exposed. Layer dip direction is represented by the orientation of the symbol and the number next to the symbol is the dip angle. Thin contour lines are at 10 m interval and thick contour lines are at 100 m interval.

all of these layered deposits occur as high standing mounds inside the craters either as central peaks or near where uplifted areas would be expected. These layered deposits are also found adjacent to massive materials that are uplifted as the central peak or exposed rim. Thirdly, the phyllosilicate detection in Kalpin crater indicates water-rock interactions either pre-dating the crater formation or linked to impact-related hydrothermal processes. If this alteration post-dates the impact crater, we would expect a more widespread alteration within the crater, but the hydrated mineral deposits are restricted to the central peak region. Finally, the higher dip angles (up to  $15.4^\circ$ ) and extensive fragmentation are consistent with impact uplifted materials.

Given these considerations, we find that an origin where the materials are uplifted by the impact craters is most consistent with the presence, distribution, and morphology of the layered deposits. Sedimentary units in the transition unit and adjacent highlands have been

mapped as Noachian-Early Hesperian in age (Tanaka et al., 2014) and the subsurface sedimentary units with hydrated minerals could have formed via subaqueous processes during the same period and have been buried beneath Amazonian lava flows in the Elysium volcanic unit. The original depth of the Kalpin crater central peak unit is likely  $>5\text{--}6$  km, as inferred from the maximum melting depth of this crater. Original depths calculated for the five other smaller craters (with diameter 13–30 km) vary from 1 to 3 km (Table 3), indicating the layered unit is present in the subsurface of at least 1 km below the surface.

#### 5.4. Inferred stratigraphy and geologic history

The overall stratigraphy of the region has younger units toward Elysium Mons (Fig. 12). We have identified a phyllosilicate bearing deposit inside Kalpin crater, the layered sediments in six impact craters,

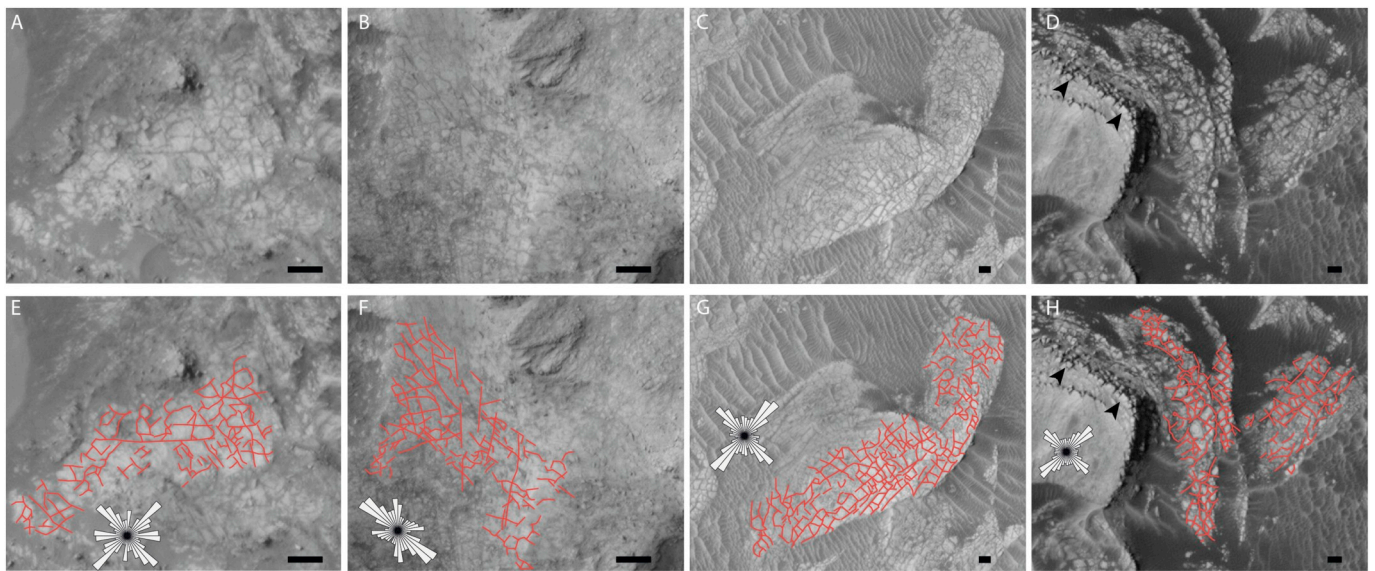


**Fig. 9.** Fractures within the layered unit exposed within impact craters mapped in HiRISE image PSP\_008305\_1890 (Kalpin crater, A, B, E, F) and ESP\_033042\_1845 (Wafra crater, C, D, G, H). A-D show the close-in image of the fractures in flat, dust and sand-free surfaces. Black scalebars are 10 m. The dark-toned fractures which are commonly 1–2 pixels wide (with width < 1 m) are mapped in red lines in Fig. E-F and a directional histogram shows the normalized histogram in the orientations of line segments mapped in red. Arrows in D, H point to steep slopes shedding decameter sized blocks following the pre-existing fractures. (For interpretation of the references to color in this figure legend, the reader is referred to the web version of this article.)

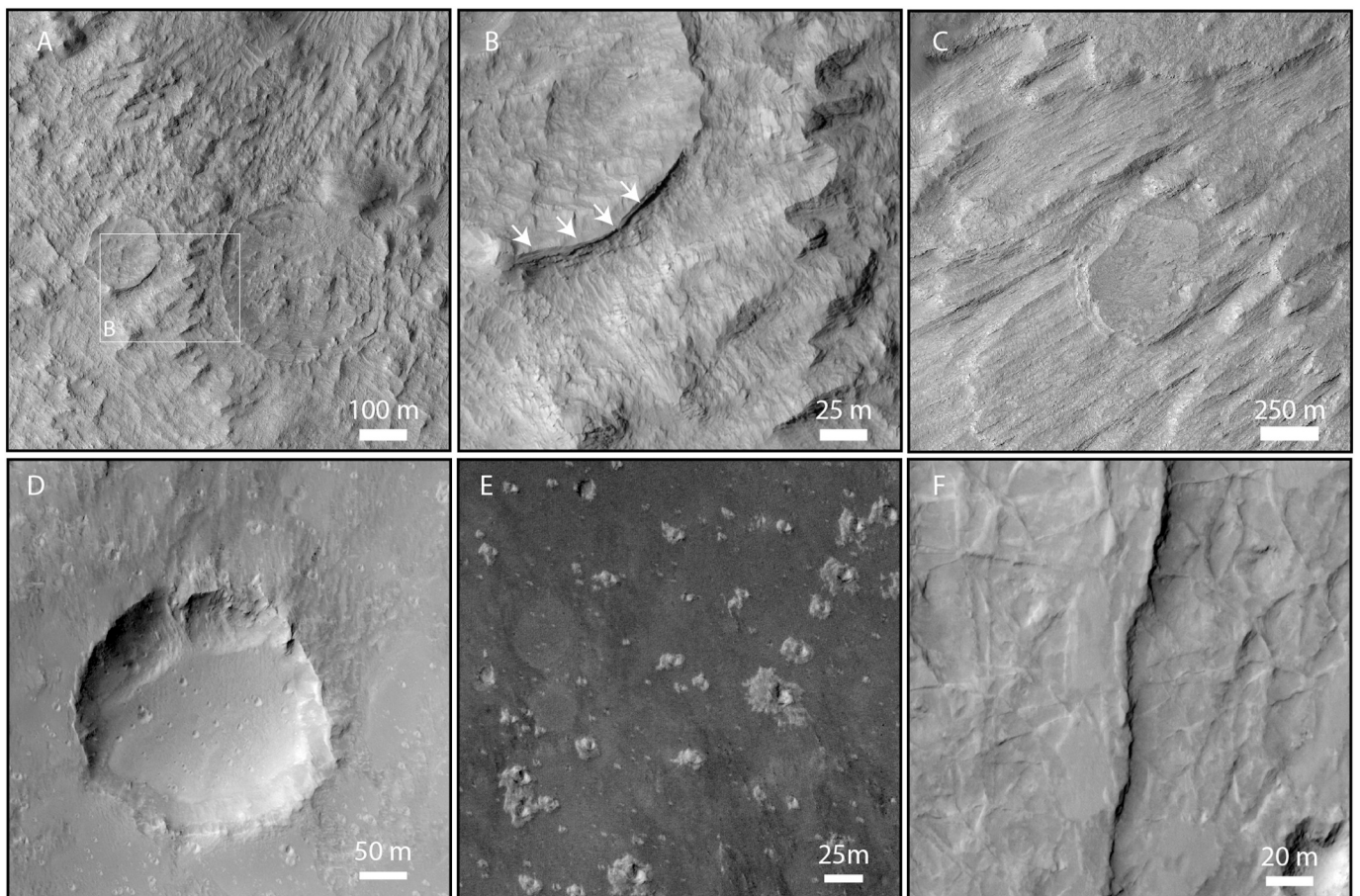


**Fig. 10.** The morphology of small buttes and mesas in the transition unit. The locations are indicated in Fig. 8. A-B: Embedded impact craters filled with erodible, layered sedimentary deposits (HiRISE image ESP\_019553\_1800), B is a subset of Fig. A showing the details of the layered deposit; C: Particular erosional landform with embedded impact craters (HiRISE image PSP\_006275\_1800); D–F: Small mound in the transition unit with embedded crater (D), small craters with bright, irregular ejecta blanket (E) and ridge morphology (F). D–F are subsets from HiRISE image PSP\_008648\_1810. HiRISE images shown here are stretched to show the internal contrast (albedos are not comparable between images).

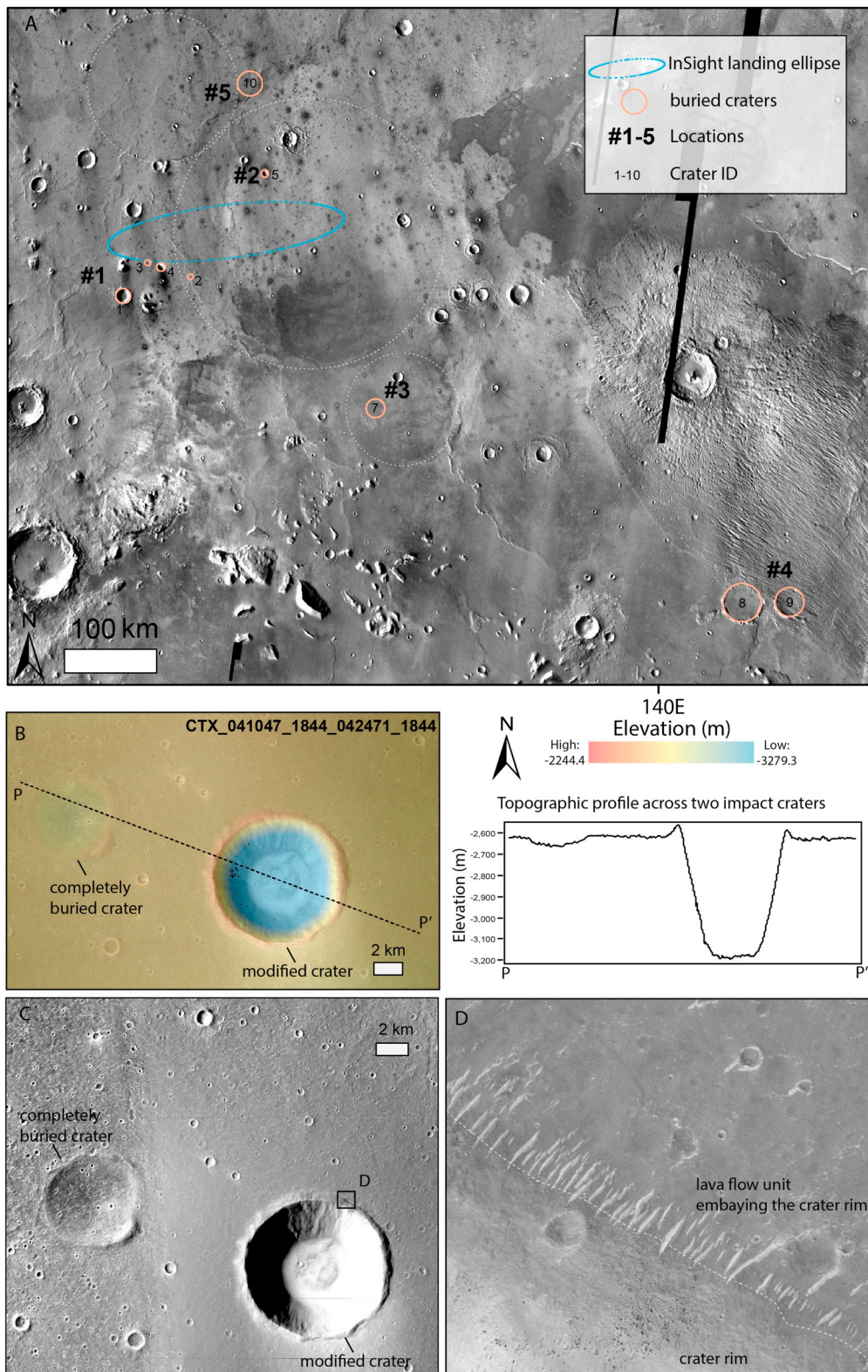


**Fig. 11.** A. Locations of partially buried impact craters in Table 2 in the vicinity of the InSight landing ellipse. White dotted circles show the locations of quasi-circular depressions indicating possible buried impact basins (Golombek et al., 2018). B–D: Type example of almost completely buried (Crater 3) and partially buried impact craters (Crater 4) in the landing site region. B. Digital elevation model computed from CTX stereo images ESP\_041047\_1844 and ESP\_042471\_1844 covering two small impact craters that have been almost completely buried and partially buried, respectively. PP' is the cross-section of the topography profile from this stereo pair. Note the reduced crater rim-height and buried ejecta blanket of the partially buried crater. C. CTX and HiRISE images of these two craters, with the location of C shown in the box on the crater rim. D. The detail of the contact between the lava flow unit and the crater rim. Embayment of the lava flow likely created a local depression that gathered aeolian bedforms.

**Table 2**  
Buried and modified crater morphometry measurement and infill thickness calculation.

Crater no.	Crater ID <sup>a</sup>	Type <sup>b</sup>	Diameter (km)	Cratering regime	D <sup>b</sup> (km)	H <sup>b</sup> (km)	D0 <sup>b</sup> (km)	H0 <sup>b</sup> (km)	T <sub>infill</sub> <sup>a</sup> (m)	D <sub>infill</sub> <sup>a</sup> (m)
Location #1										
1	14-000602	P	8.61	Simple	1.2	0.22	1.7	0.41	0.19	0.5
2	N. A.	C	3.07	Simple	0.09	0.01	0.79	0.17	0.15	0.69
3	15-001030	C	3.22	Simple	0.01	0.02	0.82	0.18	0.15	0.81
4	15-000590	P	4.86	Simple	0.45	0.04	1.11	0.25	0.21	0.66
								Average	0.18	0.66
Location #2										
5	15-000748	P	4.15	Simple	0.48	0.06	0.99	0.22	0.16	0.51
								Average	0.16	0.51
Location #3										
7	15-000244	C	10.83	Complex	0.04	0.03	1.04	0.62	0.59	1
								Average	0.59	1
Location #4										
8	15-000079	C	16.9	Complex	0.24	0.12	1.19	0.74	0.63	0.96
9	15-000123	C	23.04	Complex	0.24	0.29	1.31	0.84	0.56	1.07
								Average	0.59	1.01
Location #5										
10	15-000154	C	14.24	Complex	0.08	0.07	1.13	0.69	0.62	1.05
								Average	0.62	1.05

<sup>a</sup> The corresponding ID in Mars global crater database in (Robbins and Hynek, 2012) is indicated in the table. N. A. indicates the crater is not available in the database.

<sup>b</sup> Type: Letter denotes the crater is partially buried (P) or almost completely buried (C). D: Rim-to-floor depth; H: Rim height; D<sub>0</sub>: Calculated crater depth; H<sub>0</sub>: Calculated rim height; T<sub>infill</sub>: Infill thickness outside the crater; D<sub>infill</sub>: Infill thickness within the crater.

**Table 3**  
Calculation of original depths for materials exposed in impact craters.

Exposed materials	Crater ID <sup>a</sup>	Figure	Crater size (km) <sup>a</sup>	Location of outcrop	Maximum excavation depth (km)	Maximum melting depth (km)		Structural uplift (km)
						Croft	Holsapple	
Olivine, pyroxene		3	1.5–7	Crater rim	0.13–0.54			
Fe/Mg								
phyllosilicate	15-000018	4	50.8	Central peak		6.4	5.3	4.9
	15-000018	7A	50.8	Central peak		6.4	5.3	4.9
	15-000048	7F	29.9	Central peak		3.6	2.8	2.9
	15-000119	7C	17.4	Central peak/crater floor	1.2	2.0	1.5	1.6
	15-000130	7B	16.1	Central peak		1.8	1.4	1.5
	15-000171	7D	13.2	Crater rim	1.0			
Layered deposit	15-000174	7E	13.0	Crater rim	0.9			

<sup>a</sup> From Mars crater database (Robbins and Hynek, 2012).

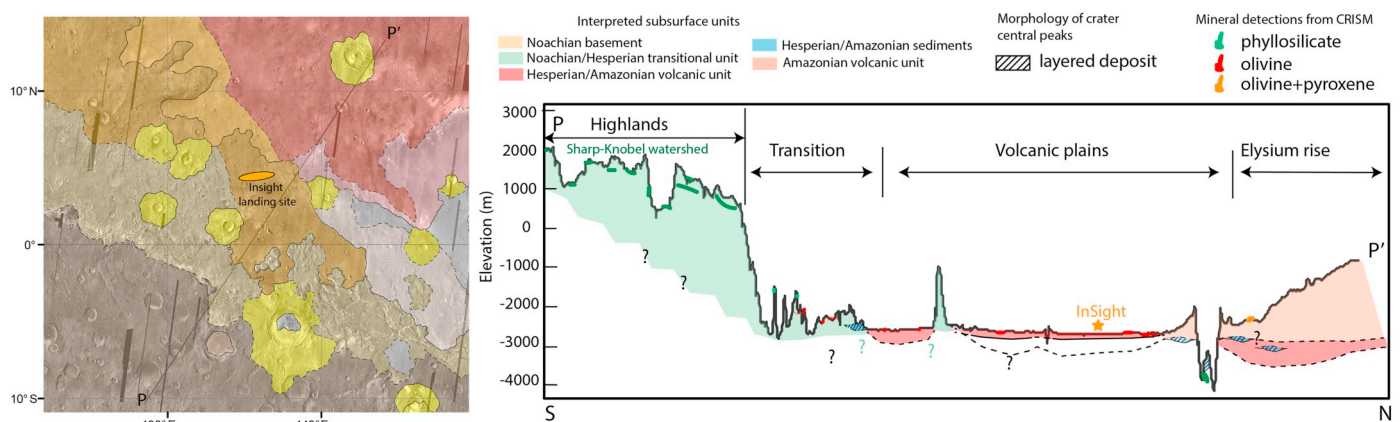


**Fig. 12.** A proposed cross-section (P-P') based on the mineralogy observation and layered morphology of the central peaks, with the geological context of the profile given on the left.

as well as widespread sedimentary processes within the transition unit. Although the full spatial extent and thickness cannot be well resolved given the limited exposures, the observation of various lithologies and

sedimentary units in the surrounding region supports subsurface units beneath the InSight lander that could be detected seismically. Synthesizing our observations together with previous work (Irwin et al., 2004;

Kerber and Head, 2010; Tanaka et al., 2005, 2014; Head et al., 2002; Golombek et al., 2017, 2018), we propose a geologic history of the landing site region influenced strongly by the topographic dichotomy (Fig. 13). The northern lowlands probably shared the same clay-bearing basement materials as the southern highlands in the Noachian during which fluvial activity was widespread (Carter et al., 2010; Pan et al., 2017). During the Early Hesperian, Medusae Fossae units start to form along the dichotomy with increasing elevation toward the highlands. Then strong deflation and denudation along the dichotomy shaped the sedimentary landforms in the transition units. In the mid-late Hesperian, multiple episodes of lava flows were emplaced and embayed the sedimentary units in the transition zone, masking earlier strata in the lowlands. Volcanic activity continued in the Early Amazonian, during which only aeolian erosion was the main active process in shaping the morphology of the limited exposures of sedimentary units along the dichotomy. This schematic evolutionary history of the region indicates the clay-bearing basement and MFF units could be rather widespread beneath the lava flows. The presence of these diverse geologic units in the subsurface of the landing site results in elastic properties variations which may influence seismic wave propagation depending on their density/velocity contrasts and spatial extent.

### 5.5. Implications for seismic profiles and InSight

The observations of the clay-bearing deposits in Kalpin crater and the transition unit, as well as the possible widespread distribution of Medusae Fossae Formation imply the existence of altered and sedimentary units beneath the lava flow units where InSight is located in. Several other independent observations also indicate the possible existence of a weak layer beneath the 200–300 m thick basaltic lava flows (Golombek et al., 2017, 2018; Warner et al., 2017). Potential seismic profiles have been proposed, focusing on the regolith as well as the first 40 m stratigraphy transitioning from the ~10 m thick relatively sandy regolith layer to coarse breccia to basement basaltic flows with depth (Golombek et al., 2017; Knappmeyer-Endrun et al., 2017, 2018; Morgan et al., 2018). Here our results suggest the possible seismic responses of a weak layer from 200 to 300 m up to kilometers in depth in the subsurface of the landing site should also be considered. Combined with previously-established near-surface stratigraphy (Golombek et al.,

2017) and seismic velocity profiles (Knappmeyer-Endrun et al., 2017), testable seismic profiles for the landing site vicinity could be proposed based on physical properties of martian meteorites as well as terrestrial analogs.

We propose 6 crustal models (Fig. 14) for future consideration and seismic data analysis (e.g. Tauzin et al., in prep) based on these a priori geological constraints. For the first 40 m below the surface, Knappmeyer-Endrun et al. (2018) provide the seismic velocity and density profile based on the laboratory work from Delage et al. (2017) and an analogy to the Cima Volcanic Field on Earth. At depth, we use the seismic properties from analog rocks from Earth including basalt, sandstone/siltstone/clay, and martian meteorites, and interpolate between the different layers for transitional sections. Under Mars relevant conditions (0–10% porosity and heat flow of 6–30 mW/m<sup>2</sup>), the amplitude of wave velocities variations due to pressure and temperature ( $1.14 \times 10^{-2}$  km/s for Vp and  $1 \times 10^{-3}$  km/s for Vs) in the first 5 km of the crust are negligible. The depth of the possible low-velocity materials is not well constrained, with an upper limit of –200 to –300 m indicated by the cut off diameter of rocky ejecta craters (Golombek et al., 2018), and a lower limit of –1 to –5 km from the excavation depths of impact craters that expose layered deposits and phyllosilicates. We here assume the lava flow layer reaches a depth of 250 m in the shallow models (models 1–3) and 1 km in the deep models (models 4–6), but a wider range of depths and seismic velocities should be considered in forward seismic modeling relevant to data analysis. Considering the uncertainties of the extent and thicknesses of the possible weak layer beneath the landing site, we suggest that different scenarios should be considered, including 1) a thin, weak layer (possibly sedimentary in origin) with a confined thickness sandwiched between much stronger, lava flow units and ancient crust, resulting in a strong seismic velocity contrast with the adjacent strata (e.g. model 1, 4); 2) a weak layer as an extension from the subsurface crust, heavily cratered and altered on the surface before the emplacement of lava flows, in which case the weak layer may have an intermediate seismic velocity but extends to deeper depths (e.g. model 2, 5) and 3) a direct, gradual transition from the ancient crust to the basaltic lava flows without the presence of a weak layer if the weak layer is too small or not present below the lava flows (e.g. model 3, 6). We provide these six profiles of elastic properties (density, Vp and Vs) in the supplementary information. Based on the evolution history presented

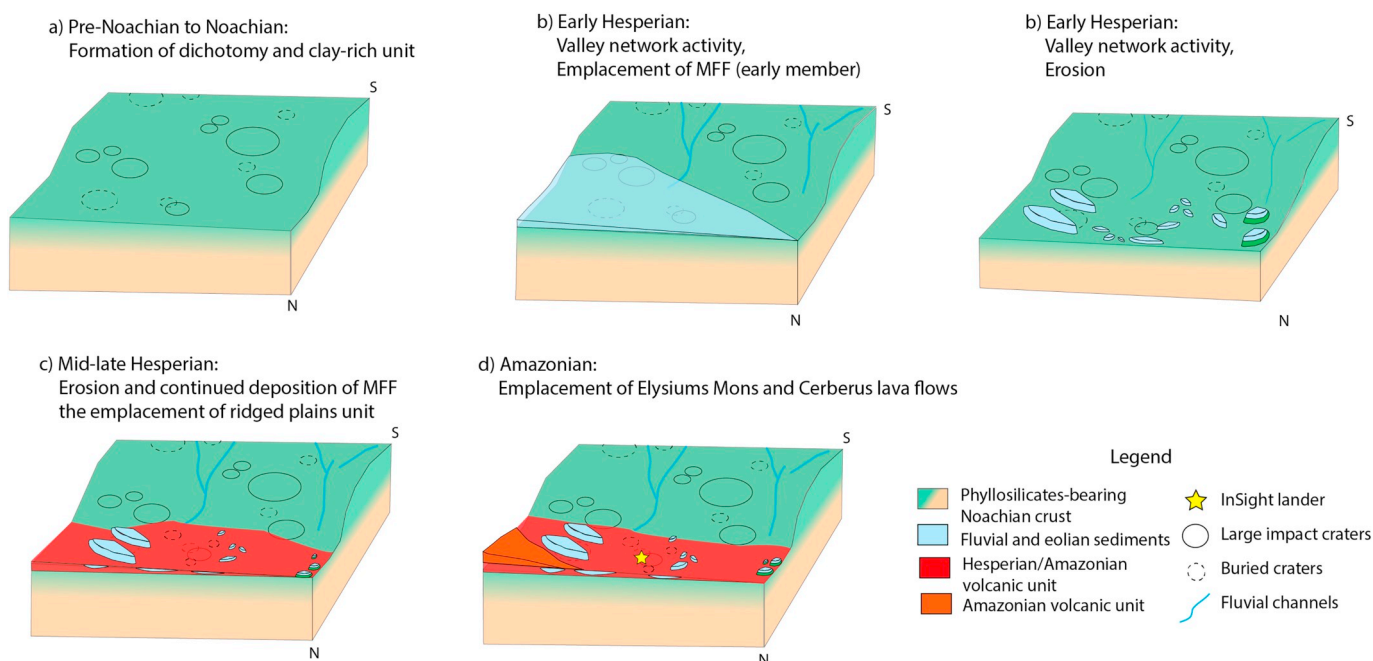


Fig. 13. A 3D-schematics of the geologic history of the landing site region.

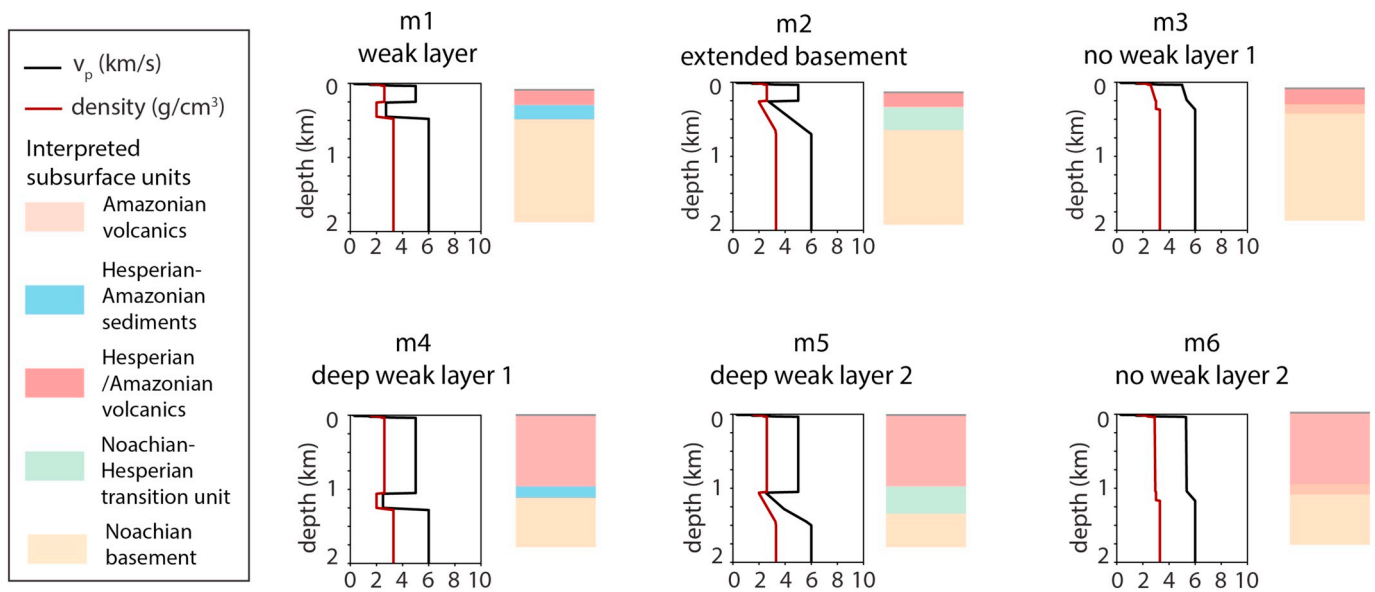


Fig. 14. Proposed schematic shallow crust models and their density and seismic wave velocity profiles.

(Fig. 13), the geologic structure in the subsurface may also indicate discrepancies in high-frequency seismic signals from marsquakes or impacts originated in the northern lowlands and southern highlands.

The subsurface structure at the InSight landing site could be further corroborated using geophysical data, including gravity and magnetic field analysis which may give insights to structures deeper than what has been discussed. With future detections of new impact craters by InSight (Daubar et al., 2018), one-dimensional crust and mantle velocity structure along the ray path could be interpreted from seismic inversion. Morphology and mineralogy of those fresh impacts will be also investigated from orbit and possibly added to the present catalog in order to bring new constraints on the crustal properties near the InSight landing site. These future investigations into the physical properties and potential layering of the Martian crust immediately beneath the InSight lander may help illuminate the origin of the dichotomy and the subsequent modifications of the Martian crust.

## 6. Conclusions

In this study, we have investigated the possible lithologies beneath the InSight landing site using a combination of orbital imagery datasets of the mineralogy and morphology of impact craters. These observations improve our understanding of the composition and physical properties of possible subsurface materials. Our main conclusions are:

1. Olivine and pyroxene spectral signatures found in association with small impact craters in the landing site region are consistent with the interpretation of the Hesperian-Early Amazonian ridged plains unit as basaltic lava flows.
2. The 51-km Kalpin crater exposed Fe/Mg clay-bearing altered basement from beneath the lava flows, indicating at least part of the subsurface stratigraphy beneath the lava flows has interacted with and has been altered by liquid water.
3. Layered, cliff-bench morphology has been identified in the interior of six impact craters, indicating that sedimentary rocks probably extend to at least 300 km north of the dichotomy, buried beneath lava flows.
4. Friable and layer-forming sedimentary units in the transition unit between the highlands and lowlands have been mapped, indicating a part of the transition zone is composed of sedimentary materials.
5. Based on regional geological evolution, we suggest the possible existence of a weak layer of either clay-bearing deposits or layered, friable sedimentary rocks 200–300 m beneath the volcanic plains.

6. Seismic profiles have been proposed to highlight their possible effects on the seismic waves recorded by InSight SEIS instruments.

## Acknowledgment

This project has received funding from the European Union's Horizon 2020 research and innovation program under the Marie Skłodowska-Curie grant agreement No. 751164. B.T. has received funding from the European Union's Horizon 2020 research and innovation program under the Marie Skłodowska-Curie grant agreement No. 793824. This research utilizes spectra acquired by J. Mustard and C. Pieters with the NASA RELAB facility at Brown University. We would like to thank Nick Warner and Christina Viviano for their detailed and thoughtful reviews that significantly improved this manuscript. Part of this work was supported by the French Space Agency CNES as well as the InSight Project at the Jet Propulsion Laboratory, California Institute of Technology, under a contract with the National Aeronautics and Space Administration. This is InSight Contribution No. 95.

## Appendix A. Supplementary data

Supplementary data to this article can be found online at <https://doi.org/10.1016/j.icarus.2019.113511>.

## References

- Abramov, O., Wong, S.M., Kring, D.A., 2012. Differential melt scaling for oblique impacts on terrestrial planets. *Icarus* 218 (2), 906–916.
- Banerdt, W.B., Smrekar, S., Lognonné, P., Spohn, T., Asmar, S.W., Banfield, D., et al., 2013. InSight: a discovery mission to explore the interior of Mars. In: Presented at the Lunar and Planetary Science Conference, vol. 44, p. 1915 (Retrieved from).
- Banerdt, W.B., Smrekar, S., Hoffman, T., Spath, S., Lognonné, P., Spohn, T., et al., 2017. The InSight mission for 2018. In: Lunar and Planetary Science Conference, vol. 48, p. 1896 (Retrieved from).
- Baratoux, D., Samuel, H., Michaut, C., Toplis, M.J., Monnereau, M., Wieczorek, M., et al., 2014. Petrological constraints on the density of the Martian crust. *Journal of Geophysical Research: Planets* 119 (7), 1707–1727.
- Barr, A.C., Citron, R.I., 2011. Scaling of melt production in hypervelocity impacts from high-resolution numerical simulations. *Icarus* 211 (1), 913–916.
- Becker, K.J., Anderson, J.A., Weller, L.A., Becker, T.L., 2013. ISIS support for NASA mission instrument ground data processing systems. In: Lunar and Planetary Science Conference, vol. 2013.
- Bell III, J.F., Malin, M.C., Caplinger, M.A., Fahle, J., Wolff, M.J., Cantor, B.A., et al., 2013. Calibration and performance of the Mars Reconnaissance Orbiter Context Camera (CTX). *International Journal of Mars Science and Exploration* 8, 1–14.

- Belleguic, V., Lognonné, P., Wieczorek, M., 2005. Constraints on the Martian lithosphere from gravity and topography data. *Journal of Geophysical Research: Planets* (E11), 110.
- Berman, D.C., Hartmann, W.K., 2002. Recent fluvial, volcanic, and tectonic activity on the Cerberus Plains of Mars. *Icarus* 159 (1), 1–17.
- Beyer, R.A., Alexandrov, O., McMichael, S., 2018. The Ames Stereo Pipeline: NASA's open source software for deriving and processing terrain data. *Earth and Space Science* 5 (9), 537–548.
- Bjorkman, M.D., Holsapple, K.A., 1987. Velocity scaling impact melt volume. *Int. J. Impact Eng.* 5 (1–4), 155–163.
- Boyce, J.M., Garbeil, H., 2007. Geometric relationships of pristine Martian complex impact craters, and their implications to Mars geologic history. *Geophys. Res. Lett.* 34 (16).
- Bradley, B.A., 2002. Medusae fossae formation: new perspectives from Mars global surveyor. *J. Geophys. Res.* 107 (E8), 5058.
- Broquet, A., Wieczorek, M.A., 2018. Gravitational signature of Martian volcanoes. In: 49th Lunar and Planetary Conference, vol. 2018.
- Burns, R.G., 1993. *Mineralogical Applications of Crystal Field Theory*. Cambridge University Press.
- Carter, L.M., Campbell, B.A., Watters, T.R., Phillips, R.J., Putzig, N.E., Safaeinili, A., et al., 2009. Shallow radar (SHARAD) sounding observations of the Medusae Fossae Formation, Mars. *Icarus* 199 (2), 295–302.
- Carter, J., Poulet, F., Bibring, J.-P., Murchie, S., 2010. Detection of hydrated silicates in crustal outcrops in the Northern Plains of Mars. *Science* 328 (5986), 1682–1686.
- Carter, J., Poulet, F., Bibring, J.-P., Mangold, N., Murchie, S., 2013. Hydrous minerals on Mars as seen by the CRISM and OMEGA imaging spectrometers: updated global view. *Journal of Geophysical Research: Planets* 118 (4), 831–858.
- Claerbout, J.F., 1971. Toward a unified theory of reflector mapping. *Geophysics* 36 (3), 467–481.
- Clénet, H., Pinet, P., Daydou, Y., Heuripeau, F., Rosemberg, C., Baratoux, D., Chevrel, S., 2011. A new systematic approach using the Modified Gaussian Model: Insight for the characterization of chemical composition of olivines, pyroxenes and olivine–pyroxene mixtures. *Icarus* 213 (1), 404–422.
- Croft, S.K., 1985. The scaling of complex craters. *Journal of Geophysical Research: Solid Earth* 90 (S02), C828–C842.
- Daubar, I., Lognonné, P., Teanby, N.A., Miljkovic, K., Stevanović, J., Vaubailon, J., Kenda, B., Kawamura, T., Clinton, J., Lucas, A., Drilleau, M., Yana, C., Collins, G.S., Banfield, D., Golombek, M., Kedar, S., Schmerr, N., Garcia, R., Rodriguez, S., Gudkova, T., May, S., Banks, M., Maki, J., Sansom, E., Karakostas, F., Panning, M., Fujii, N., Wooley, J., van Driel, M., Lemmon, M., Ansan, V., Böse, M., Stähler, S., Kanamori, H., Richardson, J., Smrekar, S., Banerdt, W.B., 2018. Impact-seismic investigations of the InSight mission. *Space Sci. Rev.* 214, 132.
- Delage, P., Karakostas, F., Dhemaied, A., Belmokhtar, M., Lognonné, P., Golombek, M., Cui, Y.J., 2017. An investigation of the mechanical properties of some Martian regolith simulants with respect to the surface properties at the InSight mission landing site. *Space Sci. Rev.* 211 (1–4), 191–213.
- Dickson, J.L., Kerber, L.A., Fassett, C.I., Ehlmann, B.L., 2018. A global, blended CTX mosaic of Mars with vectorized seam mapping: a new mosaicking pipeline using principles of non-destructive image editing. In: *Lunar and Planetary Science Conference*, vol. 49, p. 2480 (Retrieved from).
- Edgett, K.S., Malin, M.C., 2000. New views of Mars eolian activity, materials, and surface properties: three vignettes from the Mars Global Surveyor Mars Orbiter Camera. *Journal of Geophysical Research: Planets* 105 (E1), 1623–1650.
- Edwards, C.S., Nowicki, K.J., Christensen, P.R., Hill, J., Gorelick, N., Murray, K., 2011. Mosaicking of global planetary image datasets: 1. Techniques and data processing for Thermal Emission Imaging System (THEMIS) multi-spectral data. *J. Geophys. Res.* 116 (E10), E10008.
- Ehlmann, B.L., Buz, J., 2015. Mineralogy and fluvial history of the watersheds of Gale, Knobel, and Sharp craters: a regional context for the Mars Science Laboratory Curiosity's exploration. *Geophys. Res. Lett.* 42 (2).
- Ehlmann, B.L., Edwards, C.S., 2014. Mineralogy of the Martian surface. *Annu. Rev. Earth Planet. Sci.* 42 (1), 291–315.
- Ehlmann, B.L., Mustard, J.F., Murchie, S.L., Bibring, J.-P., Meunier, A., Fraeman, A.A., Langevin, Y., 2011. Subsurface water and clay mineral formation during the early history of Mars. *Nature* 479 (7371), 53–60.
- Ernst, C.M., Murchie, S.L., Barnouin, O.S., Robinson, M.S., Denevi, B.W., Blewett, D.T., et al., 2010. Exposure of spectrally distinct material by impact craters on Mercury: implications for global stratigraphy. *Icarus* 209 (1), 210–223.
- Folkner, W.M., Dehant, V., Le Maistre, S., Yseboodt, M., Rivoldini, A., Van Hoolst, T., et al., 2018. The rotation and interior structure experiment on the InSight Mission to Mars. *Space Sci. Rev.* 214 (5), 100.
- Frey, H.V., Roark, J.H., Shockey, K.M., Frey, E.L., Sakimoto, S.E., 2002. Ancient lowlands on Mars. *Geophys. Res. Lett.* 29 (10), 22–1.
- Garvin, J.B., Sakimoto, S.E.H., Frawley, J.J., 2003. Craters on Mars: global geometric properties from gridded MOLA. In: Presented at the Sixth International Conference on Mars, p. 3.
- Golombek, M., Kipp, D., Warner, N., Daubar, I.J., Ferguson, R., Kirk, R.L., et al., 2017. Selection of the InSight landing site. *Space Sci. Rev.* 211 (1–4), 5–95.
- Golombek, M., Grott, M., Kargl, G., Andrade, J., Marshall, J., Warner, N., et al., 2018. Geology and physical properties investigations by the InSight Lander. *Space Sci. Rev.* 214 (5), 84.
- Greeley, R., and Guest, J.E., 1987. Geologic map of the eastern equatorial region of Mars. *U.S. Geol. Surv. Misc. Invest. Ser. Map 1-1802-B*, scale 1:15,000,000.
- Grieve, R.A.F., Cintala, M.J., 1992. An analysis of differential impact melt-crater scaling and implications for the terrestrial impact record. *Meteoritics* 27 (5), 526–538.
- Grieve, R.A.F., Cintala, M.J., 1997. Planetary differences in impact melting. *Adv. Space Res.* 20 (8), 1551–1560.
- Grieve, R.A., Pilkington, M., 1996. The signature of terrestrial impacts. *AGSO J. Aust. Geol. Geophys.* 16 (4), 399–420.
- Grotzinger, J.P., Gupta, S., Malin, M.C., Rubin, D.M., Schieber, J., Siebach, K., Sumner, D.Y., Stack, K.M., Vasavada, A.R., Arvidson, R.E., Calef, F., Edgar, L., Fischer, W.F., Grant, J.A., Griffes, J., Kah, L.C., Lamb, M.P., Lewis, K.W., Mangold, N., Miniti, M.E., Palucis, M., Rice, M., Williams, R.M.E., Yingst, R.A., Blake, D., Blaney, D., Conrad, P., Crisp, J., Dietrich, W.E., Dromart, G., Edgett, K.S., Ewing, R.C., Gellert, R., Hurowitz, J.A., Kocurek, G., Mahaffy, P., McBride, M.J., McLennan, S.M., Mischna, M., Ming, D., Milliken, R., Newsom, H., Oehler, D., Parker, T.J., Vaniman, D., Wiens, R.C., Wilson, S.A., 2015. Deposition, exhumation, and paleoclimate of an ancient lake deposit, Gale crater, Mars. *Science* 350, aac7575.
- Hauber, E., Brož, P., Jagert, F., Jodłowski, P., Platz, T., 2011. Very recent and widespread basaltic volcanism on Mars. *Geophys. Res. Lett.* 38, L10201 <https://doi.org/10.1029/2011GL04730>.
- Hazen, R.M., Bell, P.M., Mao, H.K., 1978. Effects of compositional variation on absorption spectra of lunar pyroxenes. In: Presented at the Lunar and Planetary Science Conference Proceedings, vol. 9, pp. 2919–2934 (Retrieved from).
- Head, J.W., Kreslavsky, M.A., Pratt, S., 2002. Northern lowlands of Mars: evidence for widespread volcanic flooding and tectonic deformation in the Hesperian Period. *J. Geophys. Res.* 107 (E1), 5003.
- Holsapple, K.A., 1993. The scaling of impact processes in planetary sciences. *Annu. Rev. Earth Planet. Sci.* 21 (1), 333–373.
- Hynek, B.M., 2003. Explosive volcanism in the Tharsis region: global evidence in the Martian geologic record. *J. Geophys. Res.* 108 (E9), 5111.
- Irwin, R.P., Watters, T.R., Howard, A.D., Zimbelman, J.R., 2004. Sedimentary resurfacing and fretted terrain development along the crustal dichotomy boundary, Aeolis Mensae, Mars. *Journal of Geophysical Research E: Planets* 109 (9), 1–20.
- Kedar, S., Andrade, J., Banerdt, B., Delage, P., Golombek, M., Grott, M., et al., 2017. Analysis of regolith properties using seismic signals generated by InSight's HP3 penetrator. *Space Sci. Rev.* 211 (1–4), 315–337.
- Kerber, L., Head, J.W., 2010. The age of the Medusae Fossae Formation: evidence of Hesperian emplacement from crater morphology, stratigraphy, and ancient lava contacts. *Icarus* 206 (2), 669–684.
- Kiefer, W.S., 2005. Buried mass anomalies along the hemispheric dichotomy in eastern Mars: implications for the origin and evolution of the dichotomy. *Geophys. Res. Lett.* 32.
- Kirk, R.L., 2003. High-resolution topomapping of candidate MER landing sites with Mars orbiter camera narrow-angle images. *J. Geophys. Res.* 108 (E12), 8088.
- Kirk, R.L., et al., 2008. Ultrahigh resolution topographic mapping of Mars with MRO HiRISE stereo images: meter-scale slopes of candidate Phoenix landing sites. *J. Geophys. Res.* 113, E00A24.
- Knapmeyer-Endrun, B., Golombek, M.P., Ohnberger, M., 2017. Rayleigh wave ellipticity modeling and inversion for shallow structure at the proposed InSight landing site in Elysium Planitia, Mars. *Space Sci. Rev.* 211 (1–4), 339–382.
- Knapmeyer-Endrun, B., Murdoch, N., Kenda, B., Golombek, M.P., Knapmeyer, M., Witte, L., et al., 2018. Influence of body waves, instrumentation resonances, and prior assumptions on Rayleigh wave ellipticity inversion for shallow structure at the InSight landing site. *Space Sci. Rev.* 214 (5), 94.
- Kneissl, T., van Gasselst, S., Neukum, G., 2010. Measurement of strike and dip of geologic layers from remote sensing data — new software tool for ArcGIS. In: Presented at the Lunar and Planetary Science Conference, vol. 41, p. 1640 (Retrieved from).
- Konopliv, A.S., Park, R.S., Folkner, W.M., 2016. An improved JPL Mars gravity field and orientation from Mars orbiter and lander tracking data. *Icarus* 274, 253–260.
- Langlais, B., Thébaud, E., Houliéz, A., Purucker, M.E., Lillis, R.J., 2019. A new model of the crustal magnetic field of Mars using MGS and MAVEN. *J. Geophys. Res.* 124 <https://doi.org/10.1029/2018JE005854>.
- Langston, C.A., 1979. Structure under Mount Rainier, Washington, inferred from teleseismic body waves. *J. Geophys. Res.* 84 (B9), 4749.
- Li, X.-Q., Nábělek, J.L., 1999. Deconvolution of teleseismic body waves for enhancing structure beneath a seismometer array. *Bull. Seismol. Soc. Am.* 89 (1), 190–201.
- Lognonné, P., Banerdt, W.B., Giardini, D., Pike, W.T., Christensen, U., Laudet, P., et al., 2019. SEIS: Insight's seismic experiment for internal structure of Mars. *Space Sci. Rev.* 215 (1), 12.
- Malin, M.C., 1979. Mars: evidence of indurated deposits of fine materials. In: Presented at the Second International Colloquium on Mars, vol. 2072 (Retrieved from).
- Malin, M.C., 2000. Sedimentary rocks of early Mars. *Science* 290 (5498), 1927–1937. <https://doi.org/10.1126/science.290.5498.1927>.
- Malin, Michael C., Bell, J.F., Cantor, B.A., Caplinger, M.A., Calvin, W.M., Clancy, R.T., et al., 2007. Context camera investigation on board the Mars Reconnaissance Orbiter. *J. Geophys. Res.* 112 (E5), E05S04.
- Mandt, K.E., de Silva, S.L., Zimbelman, J.R., Crown, D.A., 2008. Origin of the Medusae Fossae Formation, Mars: insights from a synoptic approach. *J. Geophys. Res.* 113 (E12), E12011.
- McEwen, A.S., Eliason, E.M., Bergstrom, J.W., Bridges, N.T., Hansen, C.J., Delamere, W. A., et al., 2007. Mars Reconnaissance Orbiter's high resolution imaging science experiment (HiRISE). *J. Geophys. Res.* 112 (E5), E05S02.
- Melosh, H.J., 1989. *Impact Cratering: A Geologic Process* (Retrieved from).
- Milliken, R.E., Grotzinger, J.P., Thomson, B.J., 2010. Paleoclimate of Mars as captured by the stratigraphic record in Gale Crater. *Geophys. Res. Lett.* 37 (4).
- Morgan, G.A., Campbell, B.A., Carter, L.M., Plaut, J.J., 2015. Evidence for the episodic erosion of the Medusae Fossae Formation preserved within the youngest volcanic province on Mars. *Geophys. Res. Lett.* 42, 7336–7342. <https://doi.org/10.1002/2015GL065017>.

- Morgan, P., Grott, M., Knapmeyer-Endrun, B., Golombek, M., Delage, P., Lognonné, P., et al., 2018. A pre-landing assessment of regolith properties at the InSight landing site. *Space Sci. Rev.* 214 (6), 104.
- Murchie, S., Arvidson, R., Bedini, P., Beisser, K., Bibring, J.-P., Bishop, J., et al., 2007. Compact Reconnaissance Imaging Spectrometer for Mars (CRISM) on Mars Reconnaissance Orbiter (MRO). *J. Geophys. Res.* 112 (E5), E05S03.
- Murchie, S.L., Mustard, J.F., Ehlmann, B.L., Milliken, R.E., Bishop, J.L., McKeown, N.K., et al., 2009. A synthesis of Martian aqueous mineralogy after 1 Mars year of observations from the Mars Reconnaissance Orbiter. *J. Geophys. Res.* 114, E00D06.
- Mustard, J.F., 2005. Olivine and pyroxene diversity in the crust of Mars. *Science* 307 (5715), 1594–1597.
- Ody, A., Poulet, F., Bibring, J.-P., Loizeau, D., Carter, J., Gondet, B., Langevin, Y., 2013. Global investigation of olivine on Mars: insights into crust and mantle compositions. *J. Geophys. Res. Planets* 118 (2), 234–262.
- Ojha, L., Lewis, K., 2018. The density of the Medusae Fossae Formation: implications for its composition, origin, and importance in Martian history. *J. Geophys. Res. Planets* 123, 1368–1379.
- Okubo, C.H., 2010. Structural geology of Amazonian-aged layered sedimentary deposits in southwest Candor Chasma, Mars. *Icarus* 207 (1), 210–225.
- Owens, T.J., Zandt, G., Taylor, S.R., 1984. Seismic evidence for an ancient rift beneath the Cumberland Plateau, Tennessee: a detailed analysis of broadband teleseismic *P* waveforms. *Journal of Geophysical Research: Solid Earth* 89 (B9), 7783–7795.
- Owens, T.J., Taylor, S.R., Zandt, G., 1987. Crustal structure at Regional Seismic Test Network stations determined from inversion of broadband teleseismic *P* waveforms. *Bull. Seismol. Soc. Am.* 77 (2), 631–662.
- Pan, L., Ehlmann, B.L., Carter, J., Ernst, C.M., 2017. The stratigraphy and history of Mars' northern lowlands through mineralogy of impact craters: a comprehensive survey: stratigraphy of Mars' Northern Lowlands. *Journal of Geophysical Research: Planets* 122 (9), 1824–1854.
- Pasckert, J.H., Hiesinger, H., Reiss, D., 2012. Rheologies and ages of lava flows on Elysium Mons, Mars. *Icarus* 219 (1), 443–457.
- Phạm, T.-S., Tkalčić, H., 2017. On the feasibility and use of teleseismic *P* wave coda autocorrelation for mapping shallow seismic discontinuities. *Journal of Geophysical Research: Solid Earth* 122 (5), 3776–3791.
- Pierazzo, E., Vickery, A.M., Melosh, H.J., 1997. A reevaluation of impact melt production. *Icarus* 127 (2), 408.
- Pike, R.J., 1977. Size-dependence in the shape of fresh impact craters on the Moon. In: *Impact and Explosion Cratering: Planetary and Terrestrial Implications*, pp. 489–509.
- Platz, T., Michael, G., 2011. Eruption history of the Elysium Volcanic Province, Mars. *Earth Planet. Sci. Lett.* 312 (1–2), 140–151.
- Platz, T., Michael, G., Tanaka, K.L., Skinner, J.A., Fortezzo, C.M., 2013. Crater-based dating of geological units on Mars: methods and application for the new global geological map. *Icarus* 225 (1), 806–827.
- Plescia, J.B., 2004. Morphometric properties of Martian volcanoes. *J. Geophys. Res.* 109 (E3), E03003.
- Quantin-Nataf, C., Lozac'h, L., Thollot, P., Loizeau, D., Bultel, B., Fernando, J., et al., 2018. MarsSI: Martian surface data processing information system. *Planetary and Space Science* 150 (2017), 157–170.
- Robbins, S.J., Hynes, B.M., 2012. A new global database of Mars impact craters  $\geq 1$  km: 2. Global crater properties and regional variations of the simple-to-complex transition diameter. *J. Geophys. Res.* 117, E06001 <https://doi.org/10.1029/2011JE003967>.
- Rogers, A.D., Warner, N.H., Golombek, M.P., Head, J.W., Cowart, J.C., 2018. Aareally extensive surface bedrock exposures on Mars: many are clastic rocks, not lavas. *Geophys. Res. Lett.* 45 (4), 1767–1777.
- Ruff, S.W., Christensen, P.R., 2002. Bright and dark regions on Mars: Particle size and mineralogical characteristics based on Thermal Emission Spectrometer data. *J. Geophys. Res. Planets* 107 (E12), 2-1. Chicago.
- Schneider, W.A., 1978. Integral formulation for migration in two and three dimensions. *Geophysics* 43 (1), 49–76.
- Scott, D.H., Tanaka, K.L., 1982. Ignimbrites of Amazonis Planitia Region of Mars. *Journal of Geophysical Research: Solid Earth* 87 (B2), 1179–1190.
- Scott, D.H.T., Tanaka, K.L., 1986. Geologic Map of the Western Equatorial Region of Mars.
- Smith, D.E., Zuber, M.T., Solomon, S.C., Phillips, R.J., Head, J.W., Garvin, J.B., et al., 1999. The global topography of Mars and implications for surface evolution. *Science* 284 (5419), 1495–1503.
- Spohn, T., Grott, M., Smrekar, S.E., Knollenberg, J., Hudson, T.L., Krause, C., et al., 2018. The heat flow and physical properties package (HP3) for the InSight Mission. *Space Sci. Rev.* 214 (5), 96.
- Stewart, S.T., Valiant, G.J., 2006. Martian subsurface properties and crater formation processes inferred from fresh impact crater geometries. *Meteorit. Planet. Sci.* 41 (10), 1509–1537.
- Sun, V.Z., Milliken, R.E., 2015. Ancient and recent clay formation on Mars as revealed from a global survey of hydrous minerals in crater central peaks. *Journal of Geophysical Research: Planets* 120 (12), 2293–2332.
- Sunshine, J.M., Pieters, C.M., 1998. Determining the composition of olivine from reflectance spectroscopy. *Journal of Geophysical Research: Planets* 103 (E6), 13675–13688.
- Tanaka, K., 2000. Dust and ice deposition in the Martian geologic record. *Icarus* 144 (2), 254–266.
- Tanaka, Kenneth L., Skinner Jr., J.A., Hare, T.M., 2005. USGS Geologic Map of the Northern Plains of Mars. Scientific Investigations Map.
- Tanaka, K.L., Robbins, S.J., Fortezzo, C.M., Skinner, J.A., Hare, T.M., 2014. The digital global geologic map of Mars: chronostratigraphic ages, topographic and crater morphologic characteristics, and updated resurfacing history. *Planetary and Space Science* 95, 11–24.
- Tauzin, B., Phạm, T.-S., Tkalčić, H., 2019. Receiver functions from seismic interferometry: a practical guide. *Geophys. J. Int.* 1–25.
- Tornabene, L.L., Watters, W.A., Osinski, G.R., Boyce, J.M., Harrison, T.N., Ling, V., McEwen, A.S., 2018. A depth versus diameter scaling relationship for the best-preserved melt-bearing complex craters on Mars. *Icarus* 299, 68–83.
- Turner, S.M.R., Bridges, J.C., Grebb, S., Ehlmann, B.L., 2016. Hydrothermal activity recorded in post Noachian-aged impact craters on Mars. *Journal of Geophysical Research: Planets* 121 (4), 608–625.
- Vaucher, J., Baratoux, D., Toplis, M.J., Pinet, P., Mangold, N., Kurita, K., 2009. The morphologies of volcanic landforms at Central Elysium Planitia: evidence for recent and fluid lavas on Mars. *Icarus* 200 (1), 39–51.
- Viviano-Beck, C.E., Seelos, F.P., Murchie, S.L., Kahn, E.G., Seelos, K.D., Taylor, H.W., Morgan, M.F., 2014. Revised CRISM spectral parameters and summary products based on the currently detected mineral diversity on Mars. *Journal of Geophysical Research: Planets* 119 (6), 1403–1431.
- Warner, N.H., Golombek, M.P., Sweeney, J., Ferguson, R., Kirk, R., Schwartz, C., 2017. Near surface stratigraphy and regolith production in Southwestern Elysium Planitia, Mars: implications for Hesperian-Amazonian Terrains and the InSight Lander Mission. *Space Sci. Rev.* 211 (1–4), 147–190.
- Watters, T.R., Campbell, B., Carter, L., Leuschen, C.J., Plaut, J.J., Picardi, G., et al., 2007. Radar sounding of the Medusae Fossae Formation Mars: equatorial ice or dry, low-density deposits? *Science* 318 (5853), 1125–1128.
- Zharkov, V.N., Gudkova, T.V., 2016. On the model structure of the gravity field of Mars. *Sol. Syst. Res.* 50, 235–250.
- Zimbelman, J.R., Griffin, L.J., 2010. HiRISE images of yardangs and sinuous ridges in the lower member of the Medusae Fossae Formation, Mars. *Icarus* 205 (1), 198–210.
- Zimbelman, J.R., Scheidt, S.P., 2012. Hesperian Age for Western Medusae Fossae Formation, Mars. *Science* 336 (6089), 1683.
- Zuber, M.T., Solomon, S.C., Phillips, R.J., Smith, D.E., Tyler, G.L., Aharonson, O., et al., 2000. Internal Structure and Early Thermal Evolution of Mars From Mars Global Surveyor Topography and Gravity.